Evidence for chemically heterogeneous Arctic mantle beneath the Gakkel Ridge

Megan E. d'Errico, Jessica M. Warren, Marguerite Godard

Available online at www.sciencedirect.com

ScienceDirect

Geochimica et Cosmochimica Acta 174 (2016) 291–312

Geochimica et Cosmochimica Acta

www.elsevier.com/locate/gca

Evidence for chemically heterogeneous Arctic mantle beneath the Gakkel Ridge

Megan E. D'Errico [a,*], Jessica M. Warren [a,1], Marguerite Godard [b]

[a] Department of Geological Sciences, Stanford University, 450 Serra Mall, Building 320, Stanford, CA 94305-2115, USA
[b] Géosciences Montpellier, UMR 5243 CNRS-UM, Université de Montpellier, Campus Triolet, cc60, Place Eugène Bataillon, 34095 Montpellier cedex 5, France

Received 9 November 2014; accepted in revised form 21 November 2015; available online 7 December 2015

Abstract

Ultraslow spreading at mid-ocean ridges limits melting due to on-axis conductive cooling, leading to the prediction that peridotites from these ridges are relatively fertile. To test this, we examined abyssal peridotites from the Gakkel Ridge, the slowest spreading ridge in the global ocean ridge system. Major and trace element concentrations in pyroxene and olivine minerals are reported for 14 dredged abyssal peridotite samples from the Sparsely Magmatic (SMZ) and Eastern Volcanic (EVZ) Zones. We observe large compositional variations among peridotites from the same dredge and among dredges in close proximity to each other. Modeling of lherzolite trace element compositions indicates varying degrees of non-modal fractional mantle melting, whereas most harzburgite samples require open-system melting involving interaction with a percolating melt. All peridotite chemistry suggests significant melting that would generate a thick crust, which is inconsistent with geophysical observations at Gakkel Ridge. The refractory harzburgites and thin overlying oceanic crust are best explained by low present-day melting of a previously melted heterogeneous mantle. Observed peridotite compositional variations and evidence for melt infiltration demonstrates that fertile mantle components are present and co-existing with infertile mantle components. Melt generated in the Gakkel mantle becomes trapped on short length-scales, which produces selective enrichments in very incompatible rare earth elements. Melt migration and extraction may be significantly controlled by the thick lithosphere induced by cooling at such slow spreading rates. We propose the heterogeneous mantle that exists beneath Gakkel Ridge is the consequence of ancient melting, combined with subsequent melt percolation and entrapment.

1. INTRODUCTION

Oceanic crust typically has a thickness of ~6 km, consisting of basalt and gabbro, which is generated by adiabatic decompression melting beneath spreading ridges (e.g., Reid and Jackson, 1981; Chen, 1992; White et al., 1992). However, the crust is much thinner at ultraslow (<20 mm/yr) spreading ridges because of the relative importance of conductive cooling (Reid and Jackson, 1981; Cannat, 1996; White et al., 2001; Dick et al., 2003). Gakkel Ridge (Fig. 1) is the slowest spreading ridge in the world, with a full spreading rate ranging from 13 mm/yr near Greenland to 6 mm/yr at its terminus in the Arctic Ocean (Vogt et al., 1979; Coakley and Cochran, 1998). Ridge morphology is controlled by localized volcanic centers separated by amagmatic segments (Snow et al., 2002; Dick et al., 2003). Overall, Gakkel Ridge features a deeper axial valley, thicker lithosphere and decreased total volume of crust relative to faster spreading ridges (Michael et al.,

* Corresponding author.
E-mail addresses: mderrico@stanford.edu (M.E. D'Errico), warrenj@udel.edu (J.M. Warren), marguerite.godard@um2.fr (M. Godard).
[1] Department of Geological Sciences, University of Delaware, 255 Academy Street, Penny Hall, Newark, DE 19716, USA.

http://dx.doi.org/10.1016/j.gca.2015.11.017
0016-7037/

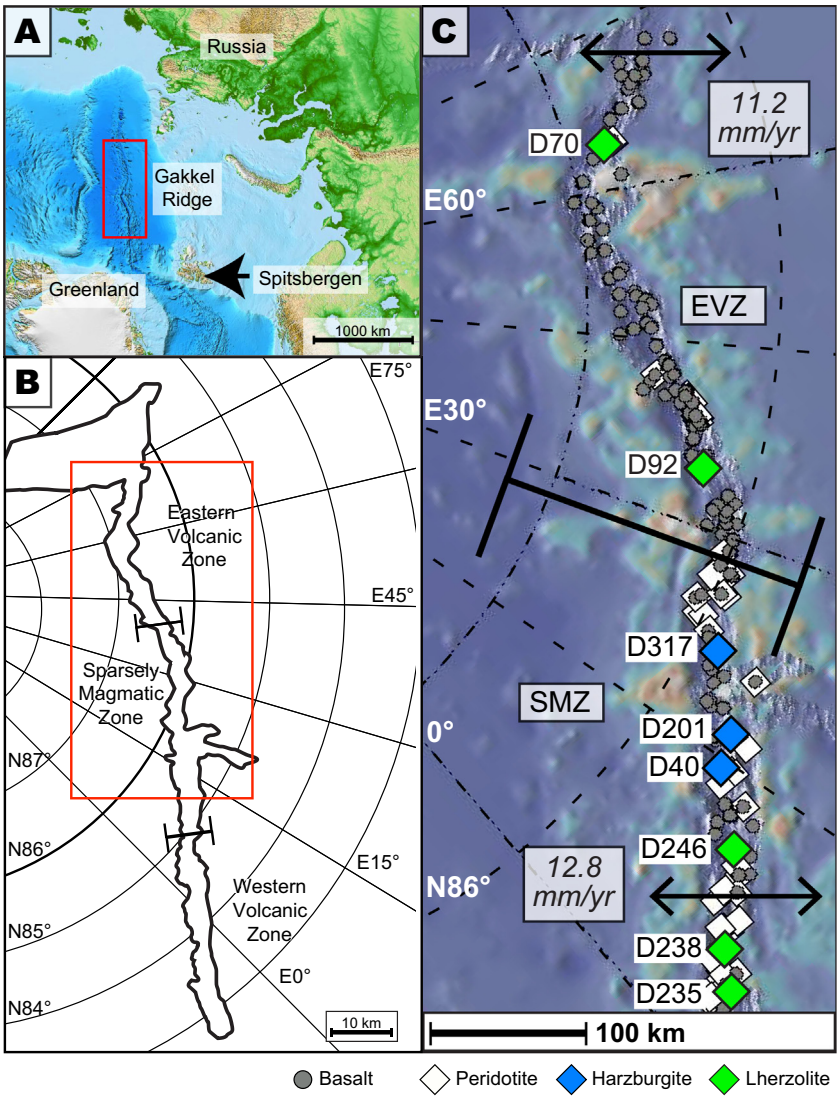

Fig. 1. (A) The location of the Gakkel Ridge in the Arctic Ocean. (B) Outline of shipboard bathymetric data collected during the AMORE cruise in 2001. Brackets indicate boundaries between the three magmato-tectonic domains of Michael et al. (2003). Area in red box is shown in detail in C. (C) Shipboard high-resolution multi-beam bathymetry data overlain on satellite altimetry data (created in GeoMapApp; Ryan et al., 2009). Dredged peridotites are marked with a diamond, with samples analyzed in this study shown as green diamonds (lherzolites) and blue diamonds (harzburgites). Locations of dredge sites are marked with a "D". Dredge numbers less than 200 refer to samples collected on the Healy (cruise HLY0102) and dredge numbers greater than 200 refer to samples collected on the Polarstern (cruise PS59). Dredged basalts are marked with a grey circle. Full spreading rates (mm/yr) are shown in italics and decrease along the ridge (Coakley and Cochran, 1998). (For interpretation of the references to color in this figure legend, the reader is referred to the web version of this article.)

2003; Jokat et al., 2003; Dick et al., 2004; Montési and Behn, 2007).

Studies of Gakkel mid-ocean ridge basalts (MORB) indicate low magma supply and a highly heterogeneous source mantle. Mühe et al. (1991, 1993, 1997) and Gale et al. (2013) published major and trace element concentration data characterizing Gakkel basalts in the context of the global MORB database. Fe and Na contents in Gakkel basalt shows extent of melting is low and suggests a low mantle temperature (Michael et al., 2004). Isotopic work on Gakkel basalts provide evidence for isotopically enriched and depleted mantle regions, suggesting that compositional heterogeneity exists beneath the ridge (Mühe et al., 1991; Mühe et al., 1993; Mühe et al., 1997; Soffer et al., 2004; Goldstein et al., 2008; Salters et al., 2012). Recent results from a U-series study demonstrate that Gakkel basalts represent the end-member product of a short melting column with shallow melt-rock reaction and subsequent melt segregation (Elkins et al., 2013). Overall, previous studies have focused on the isotopic composition of Gakkel basalts, without directly estimating the degree of mantle melting associated with variations in crustal thickness along the ridge.

Previous work on Gakkel Ridge abyssal peridotites indicate higher degrees of melting than what is expected at an ultraslow spreading ridge. Cr-spinel compositions from

Gakkel abyssal peridotites imply ~9% melting (Hellebrand et al., 2002a), which should yield a thicker crust (5.4 km) than observed (1–4 km; Coakley and Cochran, 1998; Jokat et al., 2003). The discrepancy between observed and predicted crustal thickness is suggested to result from local mantle heterogeneity due to melt focusing (Hellebrand et al., 2002a). An alternative hypothesis is that the mantle depletion is due to previous melting events (Snow et al., 2002). Supporting evidence is provided by unradiogenic $^{187}Os/^{188}Os$ ratios in Gakkel peridotites, which indicate partial melting events with ages up to 2 Ga (Liu et al., 2008). Ancient Os model ages also correspond to Hf isotopic depletions in Gakkel pyroxenes, which probably reflects the same previous melting event (Stracke et al., 2011). Interpretations presented in these isotopic studies are based on two dredged Gakkel localities (D70 and D238) within the Eastern Volcanic Zone (Fig. 1B and C). Our study builds on this previous work by extending the available abyssal peridotite data and ridge coverage.

This study presents major and trace element data for 14 abyssal peridotites recovered from 8 dredge locations covering 700 km along the Gakkel Ridge (Fig. 1C). These samples encompass the full range of trace element compositions typically observed in abyssal peridotites (e.g., Johnson et al., 1990). Peridotite compositions are used to quantify the extent of melting and to characterize the composition of the mantle beneath Gakkel Ridge. In order to reconcile the origin of samples with high degrees of melt depletion with the observed thin basalt crust, we reach the conclusion that the mantle beneath Gakkel Ridge is a result of ancient melt depletion, subsequent refertilization, incomplete melt extraction and partial melting of a mineralogically heterogeneous source.

2. GEOLOGICAL BACKGROUND AND SAMPLE DESCRIPTION

The Gakkel Ridge is a divergent plate boundary in the Arctic that separates the North American and Eurasian plates (Fig. 1A). It extends for 1800 km, from the Lena Trough in the south to its terminus near the Siberian continental shelf. Spreading rate systematically decreases along the Gakkel Ridge as it approaches the North America–Eurasia pole of rotation, with the terminus of the Gakkel Ridge marked by the disappearance of a distinct plate boundary (Coakley and Cochran, 1998). Correspondingly, the full spreading rate ranges from 13 mm/yr near Greenland to 6 mm/yr (Coakley and Cochran, 1998). In comparison to other major ridge systems, Gakkel Ridge is exceptional due to its proximity to continents on all sides (Fig. 1A) and its lack of fracture zones (Cochran et al., 2003).

In the summer of 2001, the international Arctic Mid-Ocean Ridge Expedition (AMORE) conducted a detailed mapping, seismic, and sampling survey of the Gakkel Ridge (Michael et al., 2003; Jokat et al., 2003). Samples in this study with dredge numbers less than 200 were collected by the USCGC Healy (cruise HLY0102) and samples from dredge numbers greater than 200 were collected by the RV Polarstern (cruise PS59) as part of the AMORE expedition (Fig. 1C). Based on bathymetric data and dredge results, Michael et al. (2003) divided the Gakkel Ridge into three tectonic segments from west to east: the Western Volcanic Zone (WVZ), the Sparsely Magmatic Zone (SMZ) and the Eastern Volcanic Zone (EVZ) (Fig. 1B). Magmatic activity in the two volcanic zones is greater than expected, with basalts forming 80–90% of dredged material from these zones. In contrast, the SMZ yielded ~50% peridotite, with the change from magmatic to amagmatic conditions at the transition from the WVZ to the SMZ being suggested to result from a drop in spreading rate (Dick et al., 2003).

Geophysical observations constrain the thickness of oceanic crust, which is important for determining variations in mantle melt production along the ridge. Gravity models of Gakkel Ridge suggest an average crustal thickness of 3 km (Coakley and Cochran, 1998; Weigelt and Jokat, 2001). Seismic data from the AMORE cruise indicate that oceanic crustal thickness along the SMZ is 1.4–2 km and 2.2–3.3 km along both the EVZ and WVZ (Jokat and Schmidt-Aursch, 2007). The thin crust observed at Gakkel Ridge is interpreted as evidence for overall reduced melt production (Jackson et al., 1982; Jokat et al., 2003), supporting theoretical models that predict thin oceanic crust at ridges spreading <20 mm/yr (Reid and Jackson, 1981; Bown and White, 1994; White et al., 2001; Sleep and Warren, 2014).

3. METHODS

In total, 14 samples were analyzed, of which 8 are harzburgites and 6 are lherzolites. Sample dredge locations, lithology and modal mineralogy are presented in Table 1. Thin sections used for modal analyses were all large sized (75 × 50 mm), except for two samples that were standard sized (26 × 46 mm) because not enough material was available. Modal analysis and petrographic observations of thin sections were conducted on a Leica DM2500 petrographic microscope using 0.4 mm (small thin sections) or 1 mm spacing (large thin sections) for point counting.

Major element compositions of pyroxene and olivine minerals (Table 2) were determined by Electron Microprobe Analysis (EMPA) at the United States Geological Survey in Menlo Park, using a JEOL 8900 equipped with five wavelength dispersive spectrometers. Analyses were performed with either a 10 μm (pyroxene) or a 1 μm (olivine) beam at 15 kV accelerating potential and a current of 15 nA. Peak counting intervals were 10 s for Na, and 30 s for all other elements. For olivine (Table 2a), average major element concentrations were calculated from six individual point analyses. Pyroxene minerals (Tables 2b and 2c) were analyzed by ten point core-to-rim transects to average out the effects of exsolution. In addition, grains with altered lamellae were either avoided or individual points affected by alteration were discarded during post-processing due to poor totals. Major element compositions of the spinels (Table 2d) were analyzed at Stanford University using a JEOL JXA-8230 SuperProbe. Spinel Mn data were calculated without a Cr–k–β interference correction, as we did not observe a peak overlap with Mn due to the high quality detectors of the SuperProbe. SiO_2 was measured in spinel, but was below detection for all samples. All data in Table 2

Table 1
Primary modal compositions of Gakkel peridotites.

Sample	Zone	Lat	Long	Depth (m)	Mode					
					Olivine	Opx	Cpx	Sp	Points[a]	Lithology
HLY102-40-18	SMZ	85.45	14.52	4450	85.4	11.5	0.2	2.9	2197	Harzburgite
HLY102-40-56	SMZ	85.45	14.52	4508	89.0	10.0	0.9	0.1	3625[b]	Harzburgite
HLY102-40-79	SMZ	85.45	14.52	4508	86.3	11.0	0.8	1.9	2156	Harzburgite
HLY102-40-81	SMZ	85.45	14.52	4450	71.8	26.7	0.3	1.2	2218	Harzburgite
HLY102-70-75	EVZ	86.75	64.72	4129	57.1	36.5	4.8	1.6	1831	Lherzolite
HLY102-92-36	EVZ	86.25	34.70	4876	67.7	25.5	6.5	0.4	1682	Lherzolite
PS59-201-39	SMZ	85.49	17.00	3193	75.1	21.6	1.0	2.3	2123	Harzburgite
PS59-201-40	SMZ	85.49	17.00	3193	87.0	12.1	0.0	0.9	1869	Harzburgite
PS59-235-01	SMZ	84.64	4.22	4220	78.1	14.9	5.6	1.3	2320	Lherzolite
PS59-235-17	SMZ	84.64	4.22	4220	64.0	28.5	6.3	1.3	2217[b]	Lherzolite
PS59-235-18	SMZ	84.64	4.22	4220	80.0	11.4	7.5	1.1	1844	Lherzolite
PS59-238-75	SMZ	84.79	5.68	4108	64.1	26.0	8.3	1.6	1670	Lherzolite
PS59-246-01	SMZ	85.13	10.79	4450	62.2	32.8	3.1	1.9	1656	Harzburgite
PS59-317-6	SMZ	85.80	21.53	4652	67.5	27.1	3.4	2.0	1987	Harzburgite

[a] Point counts were on a 1 mm grid on 75 × 50 mm thin sections, except where noted.
[b] Point count was on a 0.4 mm grid on 26 × 46 mm thin section.

Table 2a
Major element composition of olivines, in wt%.

Sample	# grains	# spots	SiO_2	FeO	MnO	MgO	CaO	NiO	Total	Fo
HLY102-40-18	2	2	39.99	7.79	0.12	52.10	0.06	0.40	100.45	92
HLY102-40-56	2	3	40.73	8.11	0.11	52.17	0.03	0.41	101.56	92
HLY102-40-79	3	19	40.51	7.91	0.11	51.24	0.03	0.40	100.19	92
HLY102-40-81	1	5	40.72	7.77	0.13	50.48	0.03	0.44	99.56	92
HLY102-70-75	2	5	38.30	9.06	0.11	50.76	0.03	0.38	98.65	91
PS59-201-39	3	4	39.94	8.20	0.14	52.04	0.06	0.42	100.80	92
PS59-201-40	2	5	39.73	8.18	0.13	51.75	0.06	0.41	100.26	92
PS59-235-01	2	10	40.60	9.31	0.13	50.03	0.07	0.36	100.52	91
PS59-235-17	2	8	40.54	9.20	0.13	49.62	0.05	0.36	99.90	91
PS59-235-18	1	7	38.56	9.37	0.12	49.86	0.07	0.37	98.36	90
PS59-238-75	1	3	39.58	9.32	0.15	51.00	0.06	0.36	100.48	91
PS59-246-01	1	4	40.45	9.20	0.14	50.24	0.03	0.38	100.44	91

Table 2b
Major element composition of orthopyroxenes in wt%.

Sample	# Grains	# Spots	SiO_2	TiO_2	Al_2O_3	Cr_2O_3	FeO	MnO	MgO	CaO	Na_2O	Total	Mg#
HLY102-40-18	1	13	56.96	0.01	1.80	0.62	4.89	0.12	35.14	1.24	0.04	100.82	93
HLY102-40-56	1	10	56.42	0.01	2.02	0.73	5.00	0.13	34.74	1.30	0.03	100.38	93
HLY102-40-79	2	30	56.15	0.01	2.17	0.74	4.61	0.12	34.00	1.64	0.04	99.50	93
HLY102-40-81	1	11	56.42	0.01	2.03	0.64	4.86	0.12	34.53	1.57	0.01	100.19	93
HLY102-70-75	1	4	53.84	0.06	5.17	0.70	5.64	0.14	32.13	1.80	0.10	99.57	91
PS59-201-39	2	24	56.15	0.02	2.60	0.82	5.12	0.13	33.82	1.93	0.03	100.63	92
PS59-201-40	4	65	56.10	0.03	2.28	0.83	5.18	0.13	34.15	1.56	0.05	100.30	92
PS59-235-01	1	5	52.67	0.09	5.65	0.69	5.80	0.15	31.90	2.05	0.08	99.06	91
PS59-235-17	1	8	54.33	0.09	5.47	0.53	5.91	0.13	32.47	1.69	0.07	100.69	91
PS59-235-18	1	13	53.85	0.11	5.61	0.72	5.61	0.13	30.83	3.41	0.11	100.38	91
PS59-238-75	1	21	54.36	0.08	5.20	0.54	5.86	0.13	32.87	1.48	0.04	100.56	91
PS59-246-01	2	26	53.50	0.07	5.31	0.79	5.69	0.13	31.62	2.51	0.06	99.69	91
PS59-317-6	1	13	54.16	0.04	4.08	0.76	5.59	0.15	32.22	2.39	0.03	99.43	91

are the average of at least five points. An individual analysis was excluded from the final average if the calculated oxide weight percent total deviated by more than >1.5 wt.% from 100 wt.%. For the data that remained, cation totals for olivine deviated from perfect totals by 0.3% to 0.6%, for pyroxenes by 0.05% to 1%, and for spinel by 0.1% to 0.2%. *In situ* trace element concentrations of peridotite minerals (Table 3) were obtained by LA-ICPMS at Géosciences Montpellier (University of Montpellier, France). Clinopyroxene (Cpx; Table 3a), orthopyroxene (Opx; Table 3b)

Table 2c
Major element composition of clinopyroxenes in wt%.

Sample	# Grains	# Spots	SiO_2	TiO_2	Al_2O_3	Cr_2O_3	FeO	MnO	MgO	CaO	Na_2O	Total	Mg#	Cr#
HLY102-92-36	2	25	50.94	0.22	6.17	1.20	3.05	0.10	17.50	20.57	0.32	100.09	91	12
PS59-201-39	1	10	52.98	0.02	3.02	0.97	2.02	0.08	17.83	23.38	0.37	100.67	94	18
PS59-235-01	1	9	51.23	0.24	6.67	0.99	2.91	0.10	16.97	19.09	0.80	98.99	91	9
PS59-235-17	1	10	50.65	0.27	6.61	0.90	2.91	0.10	16.61	21.24	0.80	100.08	91	8
PS59-235-18	1	15	51.29	0.22	7.00	1.07	3.77	0.12	19.84	15.85	0.67	99.82	90	9
PS59-238-75	2	28	50.86	0.24	6.55	1.01	2.85	0.10	16.75	20.91	0.53	99.81	91	9
PS59-246-01	2	19	50.30	0.17	6.30	1.13	2.52	0.09	15.89	22.43	0.50	99.33	92	11
PS59-317-6	1	5	51.61	0.08	5.36	1.27	3.04	0.10	18.74	20.14	0.21	100.56	92	14

Table 2d
Major element composition of spinels in wt%.

Sample	# Of grains	# Of spots	TiO_2	Al_2O_3	Fe_2O_3	FeO	NiO	MnO	MgO	Cr_2O_3	SUM	Mg#	Cr#
HLY0102-40-18	2	11	0.05	24.52	0.00	14.85	0.07	0.20	13.49	46.99	100.17	62	56
HLY0102-40-56	2	12	0.03	29.20	0.00	14.90	0.09	0.20	13.53	41.35	99.29	62	49
HLY0102-40-79	2	12	0.04	28.04	0.00	15.23	0.07	0.22	13.70	42.84	100.14	62	51
HLY0102-70-75	2	9	0.05	54.53	0.37	11.12	0.34	0.11	18.91	14.35	99.78	75	15
HLY0102-92-36	1	9	0.09	51.13	1.25	13.01	0.31	0.16	17.49	17.01	100.44	71	18
PS59-201-39	1	8	0.03	32.10	0.00	14.56	0.12	0.21	14.43	39.16	100.61	64	45
PS59-201-40	1	9	0.08	27.07	0.00	15.45	0.06	0.23	13.25	43.12	99.27	60	52
PS59-235-01	1	11	0.07	55.62	0.00	11.34	0.30	0.11	18.95	14.02	100.41	75	14
PS59-235-17	1	6	0.07	56.42	0.00	11.01	0.36	0.12	19.20	13.54	100.72	76	14
PS59-235-18	2	10	0.08	54.80	0.57	10.84	0.34	0.10	19.17	13.85	99.75	76	14
PS59-238-75	2	12	0.07	53.61	0.38	11.19	0.35	0.12	18.66	14.71	99.09	75	16
PS59-246-01	1	12	0.03	51.19	0.71	12.58	0.31	0.14	17.55	17.05	99.56	71	18
PS59-317-6	1	6	0.04	45.97	0.89	13.69	0.24	0.16	16.53	22.80	100.31	68	25

and olivine (Table 3c) were analyzed using either polished mounts of these minerals in indium or 150 μm thick polished sections. Analyses were performed with a Thermo Scientific Element XR (eXtended Range) high resolution ICPMS. The ICPMS was coupled to a laser ablation system consisting of a Geolas (Microlas) automated platform with a 193 nm Excimer Compex 102 laser from LambdaPhysik. Ablation analyses were performed using an in-house modified 30 cm^3 ablation cell with a helium atmosphere to enhance sensitivity and reduce inter-element fractionation (Günther and Heinrich, 1999). Helium gas and ablated sample material were mixed with argon gas before entering the plasma. Trace elements analyzed were: rare earth elements (REEs), Ba, Ni, Cr, Lu, Nb, Rb, Sr, Ta, Y, Zr, and Hf. Data were collected in time resolved acquisition mode, with the background signal collected for 2 min followed by 1 min. of sample ablation. The laser energy density was set to 10 J cm^{-2} at a frequency of 8 Hz.

For data collection, we optically selected grains based on the largest and freshest available in the sample. Beam size was either 102 μm or 122 μm, except for two samples (PS59-235-17 and HLY0102-40-81) where a beam size of 163 μm was used for olivine. The ablation spot size was chosen to give the highest possible signal while avoiding hitting fractures or serpentine in the mineral. As perfect grains were not always present, we checked every analysis on each grain after analysis to determine if the spot incorporated any alteration. During data reduction, the ICPMS signal was filtered for spikes on an element-by-element basis. Some low concentration elements had more spikes and for these it was not always possible to filter out all spikes. We assessed the possibility that these spikes could be due to alteration phases that contain higher fluid mobile element concentrations. We relied on the observation that relatively abundant fluid mobile elements, such as Sr, should also show high concentrations in alteration phases and we used this element to guide our spike removal for other elements.

Data were reduced with the GLITTER software package (Van Achterberg et al., 2001), using the linear fit to ratio method. Internal standardization relative to EMPA data was done using ^{29}Si for olivine and orthopyroxene and ^{43}Ca for Cpx. For Opx, we observed a slight difference between trace element values normalized to Si versus Ca, which is not significant when plotted on log scale trace element diagrams. However, temperatures calculated using the two-pyroxene REE thermometer (Liang et al., 2013) are highly sensitive to the normalizing reference element for Opx, but not for Cpx, due to the lower concentration of Ca in the former.

The data reported in Table 3 are calculated averages for up to 5 spots per sample, made over 1–3 grains of a phase. Values that were within 1σ of the detection limit were excluded during data reduction. Detection limits depended on the day-to-day tuning of the ICPMS, laser spot size, and element being analyzed. For analyses with a 122 μm spot size, detection limits were <4 ppb for all elements (Table 3c). Elements were also considered below detection and filtered out of the dataset if the calculated average for multiple spots had a standard deviation that was larger

Table 3a
Trace element composition of clinopyroxene in ppm (LA-ICPMS).

	HLY0102-70-75	HLY0102-92-36	PS59-201-39	PS59-235-01	PS59-235-17	PS59-235-18	PS59-238-75	PS59-246-01	PS59-317-6
Rb	0.012	b.d.	0.019	0.040	0.008	0.010	0.080	b.d.	0.018
±	0.009		0.002	0.004	0.004	0.002	0.061		0.002
Ba	0.081	0.014	0.059	0.017	0.004	0.013	b.d.	0.030	0.042
±	0.058	0.004	0.004	0.006	0.002	0.006		0.017	0.021
Sr	1.825	0.067	10.840	2.590	2.141	1.544	1.959	0.919	0.215
±	0.331	0.013	0.340	0.121	0.364	0.121	0.668	0.712	0.164
La	0.016	0.001	0.225	0.082	0.072	0.056	0.004	0.019	0.001
±	0.001	0.000	0.007	0.006	0.007	0.004	0.000	0.013	0.000
Ce	0.173	0.004	0.951	0.346	0.313	0.207	0.098	0.043	0.001
±	0.005	0.001	0.030	0.023	0.023	0.007	0.007	0.013	0.000
Pr	0.058	0.010	0.196	0.080	0.096	0.065	0.067	0.029	0.001
±	0.002	0.001	0.006	0.004	0.006	0.004	0.004	0.011	0.000
Nd	0.563	0.214	1.081	0.681	0.960	0.694	0.841	0.302	0.019
±	0.010	0.010	0.036	0.042	0.040	0.020	0.045	0.116	0.002
Sm	0.467	0.322	0.201	0.611	0.761	0.569	0.650	0.313	0.082
±	0.011	0.014	0.009	0.009	0.011	0.011	0.031	0.075	0.002
Eu	0.211	0.160	0.048	0.277	0.359	0.253	0.270	0.156	0.044
±	0.004	0.006	0.002	0.009	0.016	0.002	0.006	0.041	0.002
Gd	1.014	0.804	0.102	1.254	1.409	1.154	1.304	0.988	0.353
±	0.035	0.030	0.006	0.066	0.154	0.042	0.032	0.158	0.026
Tb	0.214	0.178	0.012	0.254	0.297	0.234	0.288	0.234	0.089
±	0.004	0.006	0.001	0.003	0.009	0.010	0.005	0.019	0.005
Dy	1.740	1.498	0.067	1.995	2.312	1.833	2.355	2.058	0.845
±	0.093	0.051	0.004	0.027	0.094	0.068	0.053	0.144	0.047
Y	10.900	8.950	0.474	11.882	12.508	10.668	14.118	13.463	5.690
±	0.320	0.290	0.015	0.267	0.567	0.348	0.326	1.698	0.269
Ho	0.390	0.342	0.016	0.453	0.511	0.408	0.534	0.494	0.213
±	0.015	0.012	0.001	0.011	0.021	0.019	0.014	0.053	0.010
Er	1.195	1.002	0.067	1.348	1.483	1.210	1.584	1.607	0.695
±	0.063	0.036	0.004	0.017	0.086	0.047	0.039	0.355	0.032
Tm	0.176	0.143	0.013	0.194	0.217	0.177	0.226	0.253	0.108
±	0.010	0.005	0.001	0.009	0.009	0.009	0.009	0.072	0.010
Yb	1.173	1.000	0.116	1.309	1.419	1.140	1.511	1.879	0.743
±	0.057	0.037	0.006	0.043	0.065	0.047	0.055	0.868	0.024
Lu	0.169	0.138	0.020	0.188	0.194	0.165	0.212	0.292	0.107
±	0.005	0.005	0.001	0.006	0.006	0.011	0.008	0.168	0.002
Zr	1.163	0.430	0.295	1.258	2.243	1.862	2.270	0.623	0.031
±	0.067	0.015	0.010	0.059	0.080	0.056	0.216	0.161	0.003
Hf	0.118	0.095	0.008	0.160	0.222	0.176	0.226	0.111	0.013
±	0.009	0.006	0.001	0.022	0.008	0.015	0.030	0.038	0.002
Ta	0.0009	b.d.	0.011	0.0011	0.002	0.002	0.0007	0.004	0.0005
±	0.0002		0.001	0.0005	0.001	0.001	0.0002	0.001	0.0002
Nb	0.018	0.018	0.076	0.014	0.015	0.012	0.019	0.031	0.015
±	0.001	0.001	0.003	0.001	0.002	0.001	0.001	0.030	0.002

Error is the standard deviation of the averaged analyses. If only one measurement was made, the error is 1 sigma, based on counting statistics. Empty cells are below detection limit. Detection limit reported from 122 spot size, normalized to Ca.

than the average value. Instrument sensitivity due to analytical conditions was determined from the average across all days of repeat measurements of the synthetic NIST 612 glass (Pearce et al., 1997), with a spot size of 122 μm and normalized to ^{43}Ca. Sensitivities were 800 cps/ppm for Ni, >57,000 cps/ppm for Sr, ~5500 cps/ppm for Ba, Nd, Sm, Gd, Dy, Er, Yb, Hf and ~27,000 cps/ppm for all other elements. Precision, as constrained by reproducibility of 34 analyses of reference basalt BIR 1-G (Appendix A), varied from 5% to 14%, depending on the element and the spot size, compared to GEOREM accepted values from (Jochum et al., 2005).

4. RESULTS

4.1. Sample petrography

The peridotites in this study are classified as harzburgite or lherzolite based on their mineral modes (Table 1). Most harzburgites are essentially devoid of Cpx and were collected near 15°E in the SMZ (Fig. 1C). The lherzolites were collected in the EVZ as well as near 0°E in the SMZ. Samples exhibit variable alteration textures (Fig. 2), with the extent of serpentinization ranging from <2% up to 75%. Primary minerals of all phases are preserved despite

Table 3b
Trace element composition of orthopyroxene in ppm (LA-ICPMS).

Sample	HLY0102-40-18	HLY0102-40-56	HLY0102-40-79	HLY0102-40-81	HLY0102-70-75	HLY0102-92-36	PS59-201-39	PS59-201-40	PS59-235-01	PS59-235-17	PS59-235-18	PS59-238-75	PS59-246-01	PS59-317-6
Rb	b.d.	0.009	b.d.	0.004	0.005	b.d.	0.021	0.048	0.014	0.006	b.d.	0.015	0.008	0.007
±		0.002		0.001	0.002		0.017	0.042	0.003	0.001		0.010	0.001	0.002
Ba	b.d.	b.d.	0.005	0.009	0.007	0.009	0.014	0.035	b.d.	b.d.	0.007	0.045	0.012	0.038
±			0.001	0.003	0.004	0.001	0.007	0.029			0.003	0.034	0.002	0.003
Sr	0.272	0.236	0.190	0.429	0.042	0.041	0.334	0.709	0.054	0.030	0.044	0.198	0.035	b.d.
±	0.176	0.109	0.045	0.071	0.031	0.046	0.162	0.300	0.038	0.013	0.015	0.130	0.017	
La	0.005	0.004	0.005	0.012	0.0008	0.00056	0.004	0.010	0.0009	0.0011	0.0011	0.0013	0.0006	0.00043
±	0.003	0.002	0.001	0.001	0.0002	0.00001	0.002	0.004	0.0003	0.0001	0.0001	0.0003	0.0001	0.00002
Ce	0.018	0.010	0.014	0.033	0.004	0.0007	0.018	0.049	0.003	0.004	0.005	0.003	0.0025	b.d.
±	0.009	0.005	0.004	0.007	0.001	0.0001	0.006	0.022	0.001	0.003	0.001	0.002	0.0003	
Pr	0.003	0.002	0.0016	0.004	0.0014	0.0006	0.005	0.010	0.0009	0.002	0.0016	0.002	0.002	b.d.
±	0.001	0.001	0.0005	0.001	0.0005	0.0001	0.002	0.004	0.0004	0.001	0.0002	0.001	0.001	
Nd	0.021	0.010	0.009	0.016	0.015	0.008	0.035	0.059	0.010	0.019	0.023	0.028	0.015	0.002
±	0.010	0.004	0.002	0.005	0.002	0.002	0.016	0.026	0.003	0.010	0.003	0.011	0.003	0.001
Sm	0.008	0.005	0.005	0.005	0.021	0.016	0.009	0.025	0.016	0.020	0.027	0.034	0.021	0.005
±	0.003	0.001	0.001	0.001	0.001	0.002	0.003	0.007	0.002	0.010	0.003	0.009	0.006	0.001
Eu	0.003	0.002	0.0016	0.0015	0.010	0.009	0.003	0.008	0.008	0.012	0.015	0.017	0.011	0.003
±	0.002	0.001	0.0004	0.0004	0.001	0.002	0.001	0.003	0.004	0.004	0.002	0.004	0.001	0.001
Gd	0.020	0.010	0.010	0.008	0.062	0.053	0.010	0.048	0.049	0.085	0.083	0.134	0.076	0.022
±	0.005	0.005	0.003	0.001	0.002	0.007	0.004	0.012	0.007	0.023	0.009	0.029	0.016	0.004
Tb	0.004	0.0014	0.003	0.0009	0.018	0.016	0.0014	0.007	0.015	0.020	0.023	0.032	0.023	0.008
±	0.001	0.0004	0.001	0.0001	0.002	0.001	0.0004	0.002	0.003	0.004	0.003	0.005	0.003	0.001
Dy	0.028	0.012	0.028	0.0064	0.191	0.178	0.011	0.066	0.156	0.200	0.230	0.328	0.228	0.101
±	0.006	0.003	0.002	0.0002	0.014	0.016	0.002	0.011	0.013	0.042	0.021	0.052	0.019	0.019
Y	0.213	0.087	0.215	0.041	1.473	1.362	0.100	0.405	1.224	1.532	1.750	2.539	1.758	0.875
±	0.024	0.008	0.013	0.001	0.082	0.114	0.021	0.053	0.131	0.261	0.108	0.286	0.117	0.104
Ho	0.007	0.0033	0.007	0.0016	0.052	0.050	0.003	0.016	0.044	0.059	0.064	0.097	0.065	0.032
±	0.001	0.0003	0.001	0.0001	0.004	0.004	0.001	0.002	0.009	0.010	0.006	0.013	0.003	0.004
Er	0.029	0.013	0.031	0.0074	0.206	0.191	0.019	0.055	0.176	0.213	0.249	0.361	0.250	0.129
±	0.005	0.001	0.004	0.0001	0.021	0.017	0.004	0.007	0.023	0.032	0.027	0.044	0.007	0.017
Tm	0.006	0.0031	0.0075	0.0017	0.037	0.036	0.005	0.010	0.035	0.042	0.044	0.068	0.043	0.026
±	0.001	0.0003	0.0002	0.0002	0.003	0.001	0.001	0.001	0.003	0.004	0.002	0.006	0.002	0.005
Yb	0.057	0.033	0.076	0.0187	0.327	0.300	0.058	0.083	0.299	0.319	0.373	0.543	0.373	0.236
±	0.007	0.003	0.014	0.0003	0.012	0.013	0.011	0.010	0.022	0.027	0.028	0.042	0.010	0.026
Lu	0.012	0.008	0.014	0.0049	0.055	0.052	0.013	0.016	0.052	0.059	0.063	0.095	0.063	0.041
±	0.001	0.001	0.001	0.0001	0.004	0.001	0.002	0.002	0.005	0.002	0.003	0.009	0.003	0.007
Zr	0.203	0.112	0.222	0.110	0.209	0.090	0.066	0.644	0.156	0.342	0.360	0.558	0.092	0.010
±	0.038	0.010	0.024	0.007	0.007	0.011	0.015	0.126	0.017	0.096	0.039	0.084	0.003	0.001
Hf	0.005	0.003	0.010	0.004	0.025	0.022	0.002	0.021	0.021	0.031	0.040	0.059	0.020	0.005
±	0.002	0.001	0.003	0.001	0.001	0.005	0.001	0.006	0.004	0.008	0.003	0.008	0.002	0.001
Ta	b.d	0.0006	b.d.	0.00050	b.d.	b.d.	0.0015	0.002	b.d.	b.d.	b.d.	0.0008	0.0005	b.d.
±		0.0002		0.00004			0.0005	0.001				0.0003	0.0002	
Nb	b.d.	0.011	0.011	0.015	0.012	0.015	0.025	0.032	0.007	0.005	0.007	0.007	0.0093	0.010
±		0.001	0.002	0.003	0.001	0.009	0.007	0.011	0.001	0.001	0.001	0.001	0.0001	0.001

alteration, except for samples HLY0102-92-36 and PS59-317-6, where serpentine replaced most olivine and could not be analyzed. Grains are generally subhedral to anhedral. Harzburgites from two dredges (D40 and D235) have the lowest degrees of alteration and preserve coarse porphyroclastic fabrics (Fig. 2A). In more altered samples, olivine are preserved as small relict grains surrounded by mesh-textured serpentine (Fig. 2B). Coarse-grained Cpx are irregularly shaped, commonly with exsolution lamellae of Opx that are partially altered (Fig. 2C). Brown, anhedral spinel grains occur within silicate minerals and at grain boundaries (Fig. 2D). All samples lack magmatic veins and plagioclase was not identified in the samples in this study, though it has been found in other peridotites from some of these dredges (von der Handt et al., 2003; von der Handt, 2008). Vermicular symplectic intergrowths of pyroxene and spinel are observed in sample HLY0102-92-36 (Fig. 2E and F), but in none of the other samples.

4.2. Major and trace element geochemistry

Mineral major element compositions range in olivine forsterite content from 90 to 92 and pyroxene Mg number (Mg# = Mg/(Mg + Fe) * 100) from 90 to 94, within the range of other abyssal peridotites (Dick, 1989; Johnson et al., 1990). Opx are near end-member enstatite and Cpx are Cr-rich diopsides (Cr_2O_3~1–4%). Spinel Cr numbers (Cr# = Cr/(Cr + Al) * 100) range from 14 to 56, while

Table 3c
Trace element composition of olivine in ppm (LA-ICPMS).

Sample	HLY0102-40-18	HLY0102-40-56	HLY0102-40-79	HLY0102-40-81	HLY0102-70-75	PS59-201-39	PS59-201-40	PS59-235-01	PS59-235-17	PS59-235-18	PS59-238-75	PS59-246-01	Detection limit
Rb	b.d.	b.d.	b.d.	b.d.	0.012	b.d.	b.d.	b.d.	b.d.	b.d.	b.d.	0.007	0.0037
±					0.001							0.002	
Ba	b.d.	0.009	b.d.	b.d.	0.024	0.006	0.030	b.d.	b.d.	b.d.	b.d.	0.013	0.0031
±		0.002			0.009	0.002	0.002					0.010	
Sr	b.d.	0.013	b.d.	b.d.	b.d.	0.055	0.008	0.024	0.017	b.d.	0.0079	0.022	0.0028
±		0.001				0.053	0.004	0.001	0.001		0.0047	0.009	
La	b.d.	b.d.	b.d.	0.0006	0.0016	0.0006	b.d.	b.d.	b.d.	b.d.	b.d.	0.005	0.0003
±				0.0002	0.0009	0.0002						0.003	
Ce	0.0007	b.d.	b.d.	0.0014	0.003	0.0010	0.0011	b.d.	0.0011	b.d.		0.010	0.0005
±	0.0002			0.0002	0.002	0.0003	0.0002		0.0002			0.006	
Pr	b.d.	b.d.	b.d.	b.d.	0.0005	b.d.	b.d.	b.d.	b.d.	b.d.	b.d.	0.0011	0.0002
±					0.0002							0.0002	
Nd	b.d.	b.d.	b.d.	b.d.	0.00165	b.d.	b.d.	b.d.	0.0015	0.0018	0.0023	0.0042	0.0007
±					0.00005				0.0003	0.0005	0.0004	0.0008	
Sm	b.d.	b.d.	b.d.	b.d.	0.0016	b.d.	b.d.	b.d.	b.d.	b.d.	b.d.	0.002	0.0007
±					0.0004							0.001	
Eu	b.d.	b.d.	b.d.	b.d.	b.d.	b.d.	b.d.	b.d.	b.d.	b.d.	b.d.	0.0007	0.0003
±												0.0003	
Gd	b.d.	0.009	b.d.	b.d.	b.d.	0.0020	b.d.	b.d.	b.d.	b.d.	b.d.	b.d.	0.0017
±		0.003				0.0009							
Tb	b.d.	b.d.	b.d.	b.d.	b.d.	b.d.	b.d.	b.d.	b.d.	b.d.	b.d.	b.d.	0.0002
±													
Dy	b.d.	0.0012	0.0013	0.0012	0.0016	0.0010	0.0011	0.0019	0.0015	0.0024	0.0011	0.0037	0.0006
±		0.0004	0.0004	0.0003	0.0006	0.0001	0.0002	0.0004	0.0003	0.0009	0.0007	0.0006	
Y	0.0022	0.0012	0.0023	0.0010	0.016	0.0017	0.005	0.022	0.021	0.018	0.014	0.009	0.0006
±	0.0004	0.0003	0.0009	0.0003	0.006	0.0006	0.001	0.001	0.004	0.003	0.003	0.006	
Ho	b.d.	b.d.	b.d.	b.d.	0.0006	b.d.	b.d.	0.0007	0.0006	0.0007	0.0005	b.d.	0.0001
±					0.0002			0.0002	0.0002	0.0001	0.0003		
Er	b.d.	0.0010	0.0011	b.d.	0.0018	b.d.	0.0018	0.005	0.004	0.005	0.004	0.0026	0.0005
±		0.0001	0.0001		0.0008		0.0006	0.001	0.001	0.001	0.002	0.0007	
Tm	b.d.	b.d.	b.d.	b.d.	0.0010	b.d.	0.0005	0.0013	0.0011	0.0009	0.0016	b.d.	0.0002
±					0.0001		0.0002	0.0004	0.0003	0.0004	0.0008		
Yb	0.003	0.0020	0.0034	0.0012	0.011	0.0016	0.003	0.017	0.016	0.014	0.018	0.007	0.0007
±	0.001	0.0005	0.0006	0.0004	0.002	0.0003	0.001	0.002	0.004	0.002	0.003	0.004	
Lu	0.0007	b.d.	0.0008	b.d.	0.0029	0.0006	0.0013	0.0047	0.0042	0.0039	0.005	0.0017	0.0002
±	0.0003		0.0001		0.0009	0.0002	0.0006	0.0004	0.0006	0.0006	0.001	0.0009	
Zr	b.d.	b.d.	0.0056	b.d.	0.008	b.d.	0.004	b.d.	0.0021	b.d.	b.d.	0.011	0.0034
±			0.0015		0.001		0.001		0.0005			0.006	
Hf	b.d.	b.d.	b.d.	b.d.	b.d.	b.d.	b.d.	b.d.	b.d.	b.d.	b.d.	b.d.	0.0007
±													
Ta	b.d.	0.0012	b.d.	b.d.	b.d.	b.d.	b.d.	b.d.	b.d.	b.d.	b.d.	b.d.	0.0003
±		0.0002											
Nb	0.0011	0.0009	0.0014	0.004	0.0006	0.002	0.0017	0.0007	b.d.	0.0005	b.d.	0.003	0.0003
±	0.0004	0.0003	0.0003	0.002	0.0002	0.002	0.0006	0.0001		0.0002		0.002	

spinel Mg# ranges from 61 to 75 (Fig. 3A). Gakkel Ridge spinel compositions encompass a large range, similar to the range observed for the entire Mid-Atlantic Ridge (MAR), while a subset of harzburgites are as depleted as harzburgites from the fast spreading East Pacific Rise (EPR), based on comparison to the data compilation in Warren (submitted). Bulk rock Al_2O_3 (based on data from Craddock et al., 2013) correlates with spinel Cr# and also indicates a large compositional range (Fig. 3B), in agreement with previous studies (Hellebrand et al., 2005; Liu et al., 2008).

Mineral trace element concentrations are reported in Table 3 and compared to previous Gakkel pyroxene peridotite compositions (Hellebrand et al., 2005) in Fig. 4. Lherzolites have typical Cpx REE patterns (Fig. 4A) with similar heavy REE (HREE) concentrations (e.g., $(Dy/Yb)_N = 1.0 - 1.1$), and variable depletions in light REE (LREE) (e.g., $(La/Yb)_N = 0.001 - 0.04$). Cpx could not be analyzed in 5 of the 8 harzburgites due to low modal abundance and grain size. Of the three harzburgites in which Cpx was analyzed, Cpx in PS59-246-01 is similar to the lherzolites, while Cpx in HLY0102-317-6 is highly depleted in LREE ($(La/Yb)_N = 0.001$) and moderately depleted in HREE ($(Dy/Yb)_N = 0.285$). In contrast, Cpx from the third harzburgite, PS59-201-39, has a concave-down REE pattern ($(Dy/Yb)_N = 0.12$) with highly enriched LREE ($(La/Yb)_N = 1.34$) (Fig. 5). Hellebrand et al. (2005)

also observed Cpx patterns with enriched LREE relative to middle REE (MREE) in samples from dredges in the SMZ region of Gakkel Ridge (in particular sample HLY0102-39-3; Fig. 5).

Opx compositions (Fig. 4B) cover a wider range than previously reported for Gakkel peridotites (Hellebrand et al., 2005). Lherzolite Opx have similar compositions, with steep REE slopes ($(La/Yb)_N = 0.001 - 0.002$ and $(Dy/Yb)_N = 0.35 - 0.41$). In contrast, harzburgite Opx encompass a wide range in concentrations ($(La/Yb)_N = 0.001 - 0.45$ and $(Dy/Yb)_N = 0.23 - 0.29$). Harzburgite samples from dredges 246 and 317 exhibit REE slopes ($(La/Yb)_N = 0.001 - 0.002$) similar to lherzolites, while samples from dredges 40 and 201 are characterized by shallower REE slope ($(La/Yb)_N = 0.05 - 0.45$). Opx from PS59-201-39 again represents an outlier among all samples, with relatively enriched LREE ($(La/Yb)_N = 0.05$; Fig. 6).

Expanded trace element plots (Fig. 6) further illustrate the variations observed between samples. The Cpx of lherzolite samples display consistently positive Zr–Hf fractionations ($(Zr/Hf)_N = 0.05 - 0.10$) and wide variation in Nb–Ta ratios ($(Nb/Ta)_N = 0.3 - 1.5$). The majority of lherzolite Opx display positive Zr–Hf fractionations ($(Zr/Hf)_N = 0.07 - 0.11$). Harzburgite Opx show mostly flat Zr–Hf fractionations ($(Zr/Hf)_N = 0.23 - 0.40$) and flat Nb–Ta fractionations ($(Nb/Ta)_N = 0.8 - 1.7$), except for a positive fractionation ($(Zr/Hf)_N = 0.02$) in sample HLY0102-317-6. Like other harzburgites, sample PS59-201-39 has flat Zr–Hf fractionations in both Cpx and Opx, but Nb–Ta is positively fractionated ($(Nb/Ta)_N = 0.40$) in Cpx and flat in Opx ($(Nb/Ta)_N = 0.95$).

5. DISCUSSION

Gakkel abyssal peridotites encompass a wider compositional range than previously observed (Hellebrand et al., 2005), as demonstrated by 1–2 orders of magnitude variation in mineral trace element concentrations (Fig. 4–6). The small spatial length-scale of observed geochemical variability cannot result only from variations in degree of melting of a uniform upper mantle, as this would require thermal anomalies at unreasonably small (i.e., sub-dredge) length-scales. We hypothesize instead that the variability reflects a combination of recent ridge processes and pre-existing heterogeneities, in agreement with other studies that show evidence for previous melting event(s) (Snow et al., 2002; Dick et al., 2004; Liu et al., 2008; Stracke et al., 2011). To test this hypothesis, peridotite trace element compositions are used below to evaluate the extent of melting and resulting crustal thickness. We also use our extensive set of trace element data for pyroxenes and olivine to calculate temperatures and partition coefficients (D).

5.1. Geothermometry

A variety of thermometers are available for mantle samples, traditionally using major element mineral data (Wells, 1977; Brey and Köhler, 1990; Witt-Eickschen and Seck, 1991; Taylor, 1998; MacGregor, 2015). Some of these major element thermometers are based upon pyroxene equilibrium, but are calibrated for the garnet stability field (e.g. Brey and Köhler, 1990). Results from different major element thermometers are often inconsistent and yield systematically low temperatures for abyssal peridotite samples. A recently published ultramafic thermometer uses the REE composition of coexisting Cpx and Opx minerals to calculate equilibrium temperatures (T_{REE}; Liang et al., 2013). T_{REE} is thought to better reflect near-magmatic temperatures, as T_{REE} temperatures are usually higher than those calculated using major element thermometers (Dygert and Liang, 2015).

To apply this thermometer to our samples, we used the Excel calculator provided as supplemental material by Liang et al. (2013) and ran the calculation using all measured REE concentrations and the robust linear least squares regression. This yields closure temperatures of 1151–1273°C in Gakkel harzburgites and 1052–1421°C in the lherzolites (Table 4). We also calculated temperatures using the major element two-pyroxene thermometer (T_{BKN}; Brey and Köhler, 1990) at an assumed pressure of 1.5 GPa and the Ca-in-orthopyroxene thermometer (Brey and Köhler, 1990) as most of our harzburgites do not contain Cpx (Table 4).

In general, T_{REE} for the Gakkel peridotites is ~80°C to ~300°C higher than temperatures derived from the major element pyroxene thermometers (Fig. 7). Other applications of the REE-based thermometer to peridotites (Liang et al., 2013; Dygert and Liang, 2015) also show systematic offsets from major element thermometers. The higher temperatures recorded by T_{REE} are thought to be due to the difference in closure temperature between the trivalent and divalent cations in pyroxenes (Liang et al., 2013). A subset of Gakkel and SWIR samples are offset to even higher T_{REE} (>1350°C) and show the largest temperature difference compared to T_{BKN}. One suggestion for the abnormally high temperatures (>1350°C) is that these samples have undergone melt-rock interaction, as noted in Liang et al. (2013). In agreement with this suggestion, sample PS59-201-39 (white circle in Fig. 7) has a unique shaped trace element pattern with the highest LREE enrichment, T_{REE} of 1264°C, and the largest difference from T_{BKN} of all Gakkel samples (379°C). However, T_{REE} in sample PS59-238-75 is 1421°C, which is 328°C higher than T_{BKN}, but displays no obvious signs of melt infiltration. We are not sure of the reason for the high T_{REE}, as the REE data show a good fit to the inversion line used to define the temperature.

We also observe that two samples from dredge 235 plot to the right of the 1:1 line (Fig. 7), due to T_{BKN} values that are higher than T_{REE}. Previous observations of this dredge have found that many peridotites are plagioclase-bearing, indicating late-stage melt-infiltration (von der Handt et al., 2003; von der Handt, 2008). All samples from the dredge, which is extremely fresh, yield similar T_{REE} ranging from 1050°C to 1160°C. The higher T_{BKN} temperatures may reflect the resetting of the major element closure temperatures by a melt, while T_{REE} was more variably affected by shallow melt addition due to higher closure temperature of REE. Therefore, the timing, temperature and depth of

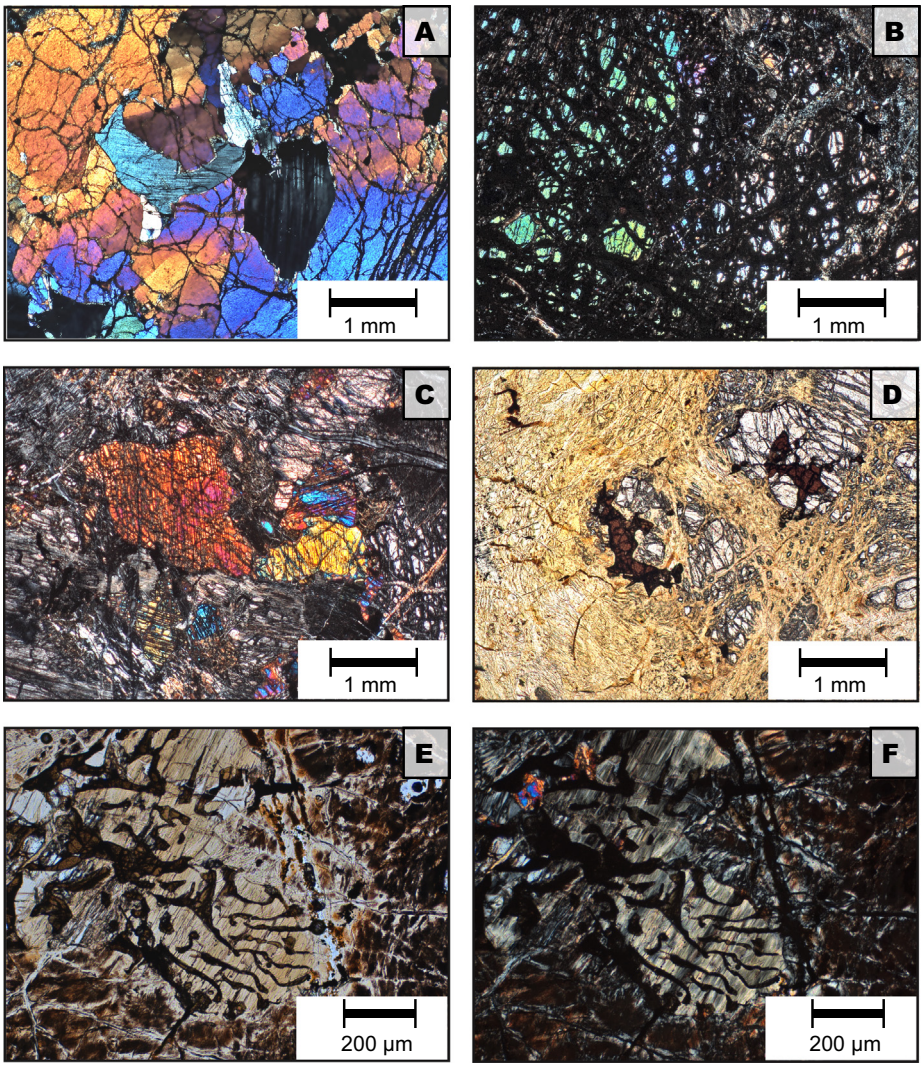

Fig. 2. Photomicrographs of Gakkel abyssal peridotites, showing the large range of fresh to altered textures. (A) Fresh, large protogranular olivine and Opx in a harzburgite (HLY0102-40-56); (B) Small olivine grains in mesh texture of serpentine (PS59-238-75); (C) Cluster of Cpx (bright colors) and Opx grains in serpentine mesh of altered olivine (HLY0102-70-75); (D) Large red-brown spinel grains associated with pyroxene (PS59-317-6); (E) and (F) Photomicrographs of pyroxene-spinel symplectite (HLY0102-92-36). All photomicrographs were taken with crossed polars, except for (D) and (E), which have open polars. (For interpretation of the references to color in this figure legend, the reader is referred to the web version of this article.)

the infiltrating melt have significant effect on recorded T_{REE} in abyssal peridotite.

Dygert and Liang (2015) used closure temperature models to show that peridotites from different tectonic settings record different cooling rates. Gakkel abyssal peridotites from this study reveal higher T_{REE} and faster cooling rates than those estimated for ophiolites (Fig. 7), further supporting the observation of Dygert and Liang (2015) that abyssal peridotites have a relatively rapid cooling rate. The Gakkel samples with the highest relative cooling rates (PS59-317-6 and PS59-238-75) are also the most altered samples in this study, which agrees with the suggestion of Dygert and Liang (2015) that hydrothermal circulation may explain the more rapid cooling of some abyssal peridotites relative to other tectonic settings.

5.2. Partitioning of LILE and HFSE

High quality data for most large ion lithophile elements (LILE, including Rb, Ba, and Sr) and high field strength elements (HFSE: including Zn, Hf, Ta, and Nb) in peridotite mineral phases is sparse due to their low concentrations. These sets of elements are useful because they are incompatible during melting, but during later processes the LILE are fluid-mobile, whereas HFSE are relatively immobile. In Fig. 8, we compare results from our study to abyssal peridotites from the Southwest Indian Ridge (SWIR; Warren et al., 2009; Seyler et al., 2011; our unpublished data) and orogenic peridotites from the Josephine Peridotite (Le Roux et al., 2014), which represent the main datasets available for peridotites. Concentrations of these

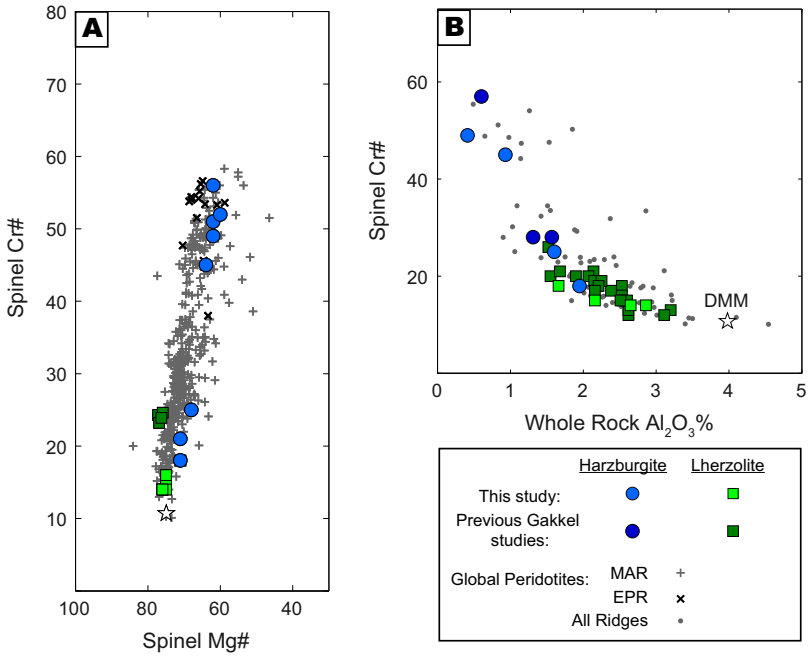

Fig. 3. Variation of spinel Cr# in Gakkel peridotites as a function of (A) spinel Mg# and (B) whole rock Al_2O_3. Data for additional Gakkel samples are from Hellebrand et al. (2002) and Liu et al. (2008). Whole rock data for samples in this study are from Craddock et al. (2013). The star indicates depleted MORB mantle (DMM) from Workman and Hart (2005). The compilation of global peridotite spinel Cr# and whole rock Al_2O_3 data are from Warren (submitted).

elements across all datasets range from 10^{-4} to 10^{2} ppm in pyroxenes and olivine (Fig. 8). Apart from Nb, the LILE and HFSE do not display distinct differences by location, though the Josephine Peridotite has a slightly narrower (e.g., Zr) or wider (e.g., Rb) concentration range in some cases. For Nb, concentrations in the Josephine Peridotite tend to be higher and span a narrower range than for abyssal peridotites.

Partition coefficients provide crucial constraints for trace element modeling of mantle melting and crustal growth processes. However, very little experimental data exists for mineral/mineral partitioning among the three mineral phases in peridotite. Here we calculate partition coefficients ($D_{Cpx/Opx}$, $D_{Cpx/Ol}$, and $D_{Opx/Ol}$) for LILE and HFSE for each of our samples (Fig. 9) and report the average of available data for natural samples (Table 5). The data for natural samples in Fig. 9 are compared to calculated mineral–mineral partition coefficients based on experimental mineral–melt partition coefficients from the compilation by Kelemen et al. (2003).

Partition coefficients calculated from the natural peridotite samples provide improved constraints on LILE and HSFE partitioning, especially for olivine. For example, the elements Nb, Zr and Hf have average partition coefficients from natural samples that overlap the partition coefficient values derived from experiments. However, $D_{Cpx/Ol}$ and $D_{Opx/Ol}$ are slightly lower in experiments, which suggests that olivine concentration data was over-estimated. Ba has noticeable differences between the previous experimental estimates and values based on natural samples, suggesting that concentrations in olivine and – to a lesser extent – orthopyroxene were previously over-estimated. Calculated partition coefficients for Nb closely match those derived from experiments.

Our partition coefficients also show good agreement among elements that are thought to behave coherently, but for which experimental data have been lacking. For example, Table 5 presents values for mineral–mineral partition coefficients for Rb and Ta, for which no experimental data are available. Rb is expected to have similar partition coefficients to Ba and the calculated average D^{Rb} is within analytical uncertainty of the calculated average D^{Ba}. Ta is expected to have similar partition coefficients to Nb and the $D_{Cpx/Opx}$ coincides for these two elements. However, $D^{Ta}_{Opx/Ol}$ is not within analytical uncertainty of $D^{Nb}_{Opx/Ol}$, while data are still not available for $D^{Ta}_{Cpx/Ol}$.

5.3. Degree of melting and amount of crust generated

The geochemical data for our abyssal peridotites indicate different extents of mantle melting among samples from individual dredges and between dredges. The low spinel Cr# of Gakkel lherzolites implies low degrees of melting, in contrast to the significantly higher spinel Cr# of some harzburgites (Fig. 3). A quantitative estimate of degree of melting for each sample can be obtained by modeling peridotite REE compositions. For this modeling, we used fractional non-modal melting equations (Shaw, 1970; Zou, 1998) with melting reaction modes from Kinzler (1997) and mineral/melt partition coefficients compiled by Kelemen et al. (2003). The composition of the depleted MORB mantle (DMM; Workman and Hart, 2005) was

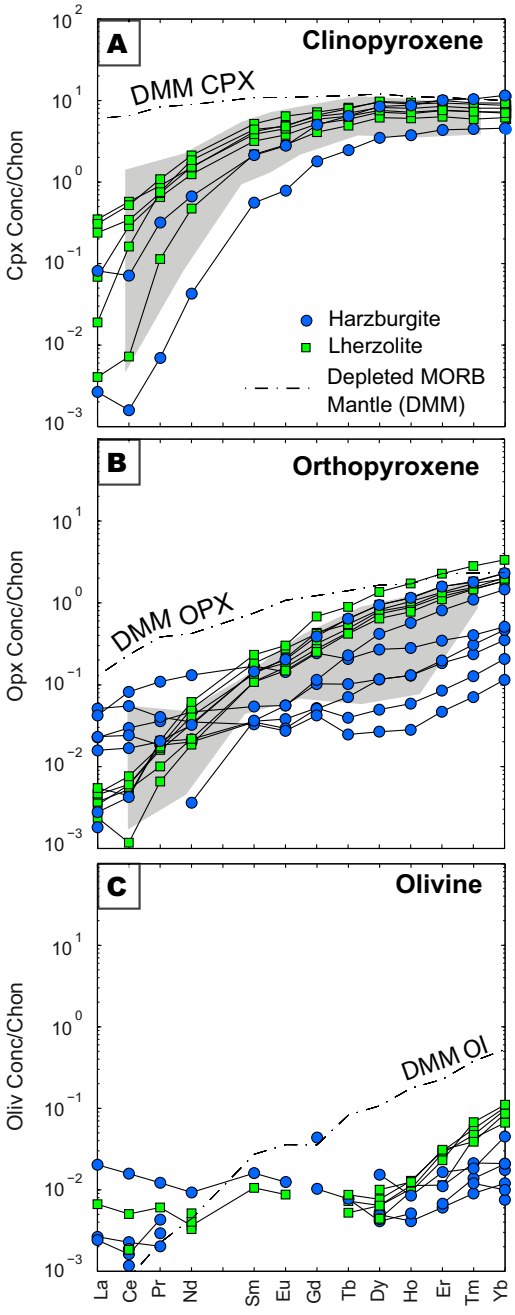

Fig. 4. Rare earth element (REE) plots of Cpx (A), Opx (B) and olivine (C). Trace element concentrations have been normalized to C1 chondrite (Anders and Grevesse, 1989). Data above the dot-dashed line are enriched relative to DMM (Workman and Hart, 2005), while data below the line are depleted. The grey field represents previous measurements of Gakkel peridotite pyroxenes (Hellebrand et al., 2005). Gaps in the REE patterns correspond to elements that were below the detection limit during a given analysis.

used as an initial composition. DMM is a hypothetical composition for the depleted upper mantle, derived from the composition of global MORB.

For the modeling, bulk rock compositions were reconstructed using mineral modes and compositions (Fig. 10).

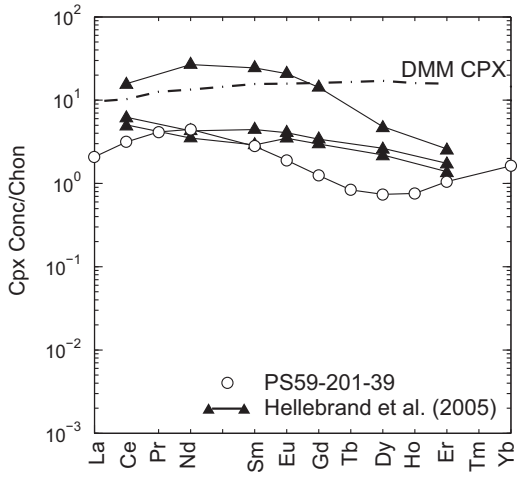

Fig. 5. REE composition of Gakkel peridotite Cpx with LREE enriched relative to MREE. The sample from this study, PS59-201-39, is shown in white circles. The black triangles correspond to harzburgite samples HLY0102-39-3, PS59-249-74 and PS59-249-79 are from Hellebrand et al. (2005).

For each sample, Cpx and Opx trace element data were used to calculate the bulk rock composition based on the equation: $M_{Ol} * C_{Opx}(D_{Ol/Opx}) + M_{Opx} * C_{Opx} + M_{Cpx} * C_{Cpx}$, where M is mode and C is concentration. For five harzburgites, Cpx was not analyzed because it was too small or not present. For these samples, Cpx was excluded from the calculation as it makes a negligible contribution to the bulk rock trace element budget. Olivine trace element concentrations were calculated by determining $D_{Ol/Opx}$ using the relevant mineral–melt partition coefficients from the compilation by Kelemen et al. (2003). Spinel was excluded from the calculation because it has negligible trace element concentrations and occurs at very low modes. The reconstructed bulk rock compositions are reported in Appendix B.

Results from modeling Gakkel lherzolite REE concentrations implies that they have undergone 4–6% fractional melting (Fig. 10A). Harzburgite HREE can be fit by 6 to ≥13% melting, but this results in modeled LREE contents that are too low relative to observed concentrations (Fig. 10B). Previous studies have documented LREE enriched patterns in harzburgites from the Mid-Atlantic, Central Indian and Southwest Indian Ridges (Hellebrand et al., 2002b; Brunelli et al., 2006; Godard et al., 2008; Brunelli et al., 2014). These studies have interpreted LREE enrichments as the result of migrating melts that intrude and interact with the residue. Our results confirm that this process also occurs at Gakkel Ridge; the effect of percolating melts is discussed below in Section 5.5.

The geochemical estimate for degree of melting can be used to estimate the amount of crust produced at the ridge. Globally, MORB chemistry suggests 10% mantle melting, which corresponds to 6 km thick crust from a melting column of 40 km height (Forsyth, 1993). However, the ultra-slow spreading rate of the Gakkel Ridge means that conductive cooling of the lithosphere terminates decompression melting at greater depth than faster ridges, causing

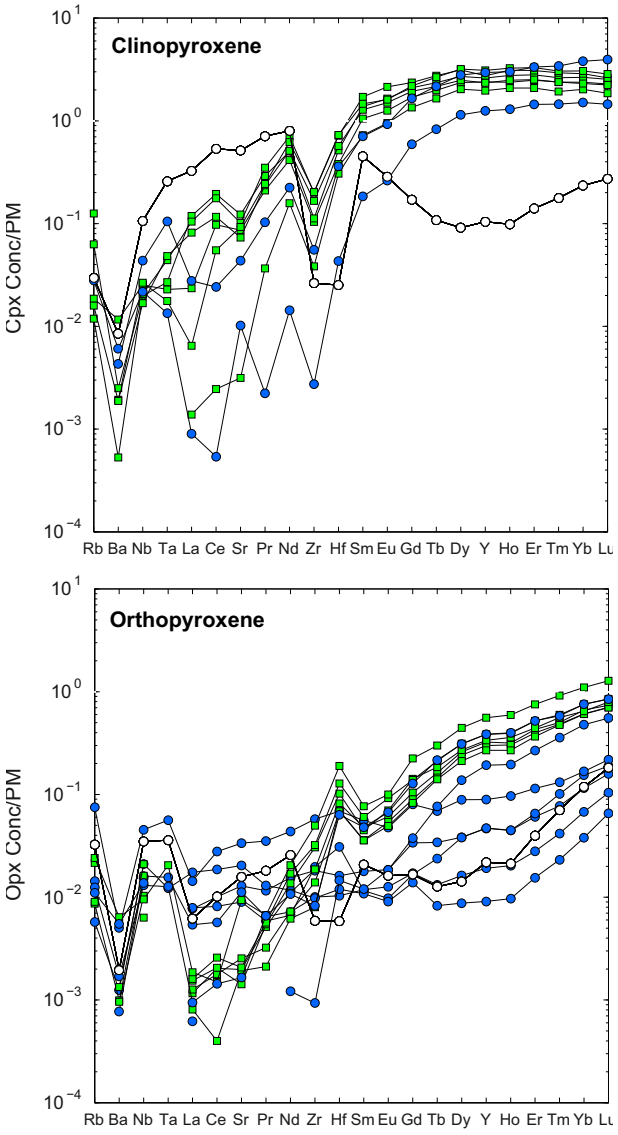

Fig. 6. Extended trace element plots normalized to primitive mantle (PM) for pyroxenes, using PM values from Sun and McDonough (1989). White circles indicate sample PS59-201-39, which has a different trace element pattern compared to all other samples in this study.

lower overall extents of melting and deeper crystallization (Reid and Jackson, 1981; Cannat, 1996; Dick et al., 2003). To estimate crustal thickness at Gakkel, we used equation 12 of Forsyth (1993), which assumes that melting occurs over a discrete depth range. The depth at which volumetrically significant melting begins is assumed to be the dry solidus at 65 km (Shen and Forsyth, 1995). Melting is estimated to terminate at 30 km depth based on the parameterization of Montési and Behn (2007) for lithospheric thickness at ultraslow ridges. The amount of crust generated is estimated based on our modeled degrees of nonmodal fractional melting (Fig. 10).

The average extent of Gakkel lherzolite melting (~5%) would produce ~6 km of crust using the Forsyth parameterization, which is the crustal thickness typical for most mid-ocean ridges. This implies that a fertile Gakkel mantle is not limited by conductive cooling, producing the same amount of crust as ridges spreading at faster rates. Harzburgite samples with HREE concentrations corresponding to 6 to ≥13% fractional melting are equivalent to 7 to ≥14 km of crust. In addition, the significant modal variation among Gakkel peridotites implies large variations in crustal thickness at <10 km length-scales.

Table 4
Temperature estimates from pyroxene thermometers.

Sample	T (REE)	Error	T (BKN)	T (Ca-in-Opx)
HLY102-40-18	–	–	–	1108
HLY102-40-56	–	–	854	1124
HLY102-40-79	–	–	–	1195
HLY102-40-81	–	–	–	1180
HLY102-70-75	–	–	–	1228
PS59-201-39	1264	42	885	1246
PS59-201-40	–	–	–	1178
PS59-235-01	1052	46	1182	1274
PS59-235-17	1163	42	1033	1203
PS59-235-18	1145	72	1317	1472
PS59-238-75	1421	37	1093	1163
PS59-246-01	1151	249	939	1347
PS59-317-6	1273	29	1190	1329

T (REE) is after Liang et al. 2013, T (BKN) and T (Ca-in-Opx) are after Brey and Kohler (1990).
Samples that do not have temperatures for T (REE) or T (BKN) are due to the fact that both Cpx and Opx were not collected in major and trace element analysis.

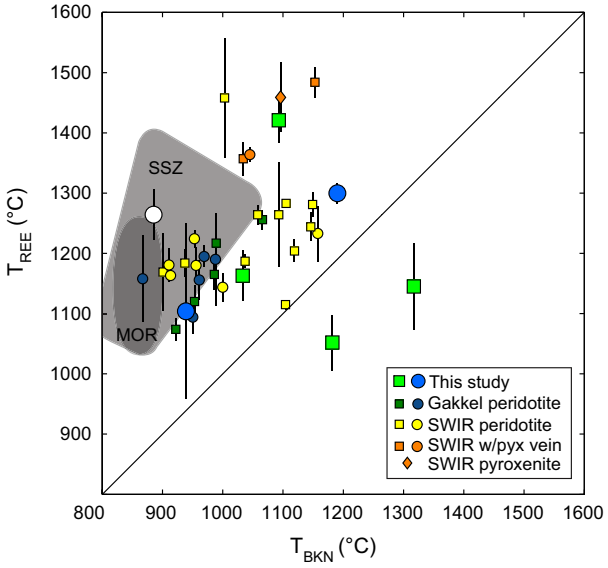

Fig. 7. Comparison between temperatures derived from the REE-in-two-pyroxene thermometer (T_{REE}; Liang et al., 2013) and those calculated using the major element two-pyroxene thermometer (T_{BKN}; Brey and Kohler, 1990). All calculations were performed assuming a pressure of 1.5 GPa. Lherzolites are plotted as squares and harzburgite as circles. Data for previous abyssal peridotite studies are from Hellebrand et al. (2005) for Gakkel and Warren et al. (2009) and Seyler et al. (2011) for SWIR.

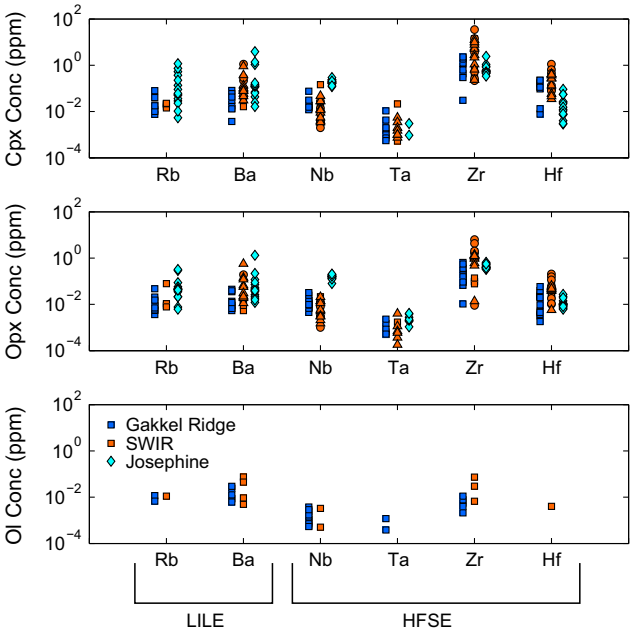

Fig. 8. Concentrations of LILE and HFSE elements in minerals from abyssal and orogenic peridotites. Data from this study for Gakkel are shown as blue squares. Also shown are SWIR data, with orange squares for our unpublished data, orange circles for Warren et al. (2009) and orange triangles for Seyler et al. (2011). Teal diamonds are for samples from the Josephine Peridotite from Le Roux et al. (2014). For this study, trace elements in olivine were below detection in many samples, whereas Warren et al. (2009) and Le Roux et al. (2014) did not measure olivine. (For interpretation of the references to color in this figure legend, the reader is referred to the web version of this article.)

The thick crust estimated based on Gakkel peridotite geochemistry is inconsistent with the on-axis thin crust observed seismically at Gakkel Ridge (Jokat et al., 2003). As a caveat, crust produced from the peridotites currently on-axis corresponds to crust that is now some distance off-axis. As estimates of off-axis crustal thicknesses are unavailable, we are assuming that crustal production has not significantly changed. Seismic measurements indicate oceanic crust in the Gakkel volcanic zones (WVZ and EVZ) is 1.4–3.3 km thick, with a maximum crustal thickness of 4.9 km above a volcanically active structure in the WVZ (Jokat and Schmidt-Aursch, 2007). The trace element composition of the most fertile Gakkel lherzolite, which corresponds to the lowest modeled amount of melting (4%), would produce 4.3 km of crust, consistent with the upper end of geophysical measurements. However, the higher degrees of melting suggested by depleted lherzolite and harzburgite compositions would produce >4.9 km of crust. In fact, Gakkel harzburgite samples with the highest degrees of implied melting (>13%) and greatest amount of predicted crust were collected where the thinnest crust (1.4–2 km) is observed, in the SMZ. The geophysical observation of crustal thickness is at least six times lower than what is predicted by harzburgite trace element geochemistry.

Mantle that has undergone previous melting event(s) can explain the discrepancy implied by refractory Gakkel harzburgites in regions of thin crust. Past events involving significant extraction of basaltic melt would produce an infertile mantle at Gakkel Ridge, preventing the generation of large amounts of crust. Modeling by Byerly and Lassiter (2014) indicates that peridotites with bulk Al_2O_3 <1 wt% produce very small amounts of melt during adiabatic decompression melting. Bulk rock major element data are available for 3 of our 6 refractory harzburgites and all 3 have <1 wt.% Al_2O_3 (Fig. 3, based on data from Craddock et al., 2013).

Evidence from the Re–Os study of Liu et al. (2008) provides additional evidence for an ancient depletion event in the mantle beneath Gakkel. Liu et al. (2008) documented unradiogenic $^{187}Os/^{188}Os$ ratios in bulk Gakkel peridotites, with model ages ranging from 50 Ma to 2 Ga. The occurrence of unradiogenic Os with 2 Ga model ages was interpreted as indicating previous melt extraction events. Other isotopic studies of peridotites have also found evidence for pre-existing isotopic depletion due to ancient melt extraction in the mantle (Harvey et al., 2006; Malaviarachchi et al., 2008; Warren and Shirey, 2012). The extent of melting calculated in this study most likely reflects the combined effects of previous melting at an ancient ridge and subsequent melting of the infertile mantle, resulting in production of thin crust at the modern Gakkel Ridge. Not all Gakkel peridotites require previous melting events based on geochemical evidence, indicating that the Gakkel mantle consists of fertile regions coexisting with more infertile components.

5.4. Length-scales of compositional variability

Underneath the ridge axis, different extents of melting can occur due to either thermal or compositional variations in the mantle. Our results demonstrate different amounts of

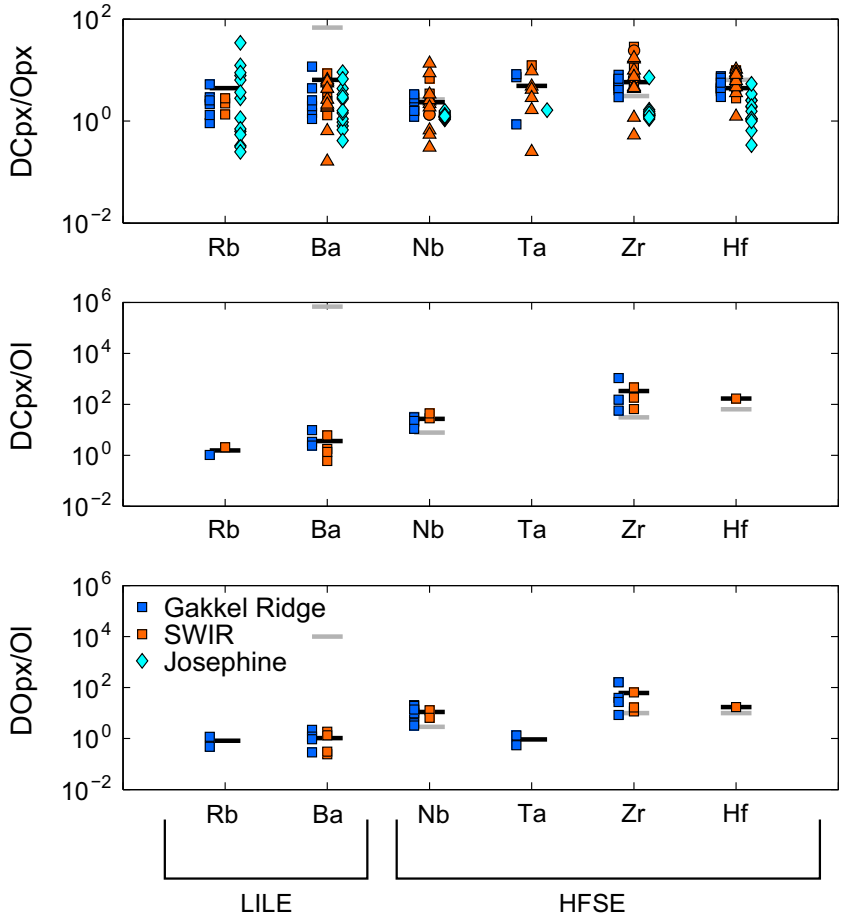

Fig. 9. Calculated mineral–mineral partition coefficients (D) of LILE and HFSE elements based on data from natural peridotites. Solid black horizontal lines indicate the calculated average of all available data compiled from natural samples. Solid grey lines indicate partition coefficients derived from mineral–melt partition coefficients measured in experiments (Hart and Dunn, 1993; Kelemen et al., 1993). The values for Ba and Hf are derived from experimental values for D^{K} and D^{Zr}, respectively (Kelemen et al., 2003).

melting among peridotites from the same dredge and among dredges in close proximity to each other (<100 km). Within a single dredge (D40), four peridotite samples have trace element concentrations that indicate a range in degree of melting of 11 to ≥13%. Similarly, the chemistries of peridotites from dredges 246 and 238 suggest 7% and 4% melting, even though they are ~60 km apart. Variation in basalt chemistry among global ridges have been attributed to large scale differences in mantle potential temperature (Klein and Langmuir, 1987; Dalton et al., 2014). Mantle temperature variations result in crossing of the mantle solidus at different depths during upwelling, which causes variation in the extent of melting. However, the observed Gakkel geochemical variability occurs at length-scales that are too short to be thermally driven, if thermal anomalies are assumed to originate deep in the mantle, for example at the core-mantle boundary.

To assess the length-scales for diffusive thermal homogenization, the approximation $x = \sqrt{\alpha t}$ is used, where x is distance, α is the thermal diffusivity constant taken as 10^{-6} m^2/s (e.g., Horai and Susaki, 1989; Gibert, 2003), and t is time. The results of this calculation show that in 1 Ma, a thermal anomaly would not persist over an area >6 km, which is greater than the distance covered by an individual dredge haul (typically <1 km). In contrast, thermal variations at >200 km scale would be preserved for

Table 5
Average partition coefficients from compilation of abyssal and orogenic peridotite studies.

	Rb	1σ	Ba	1σ	Nb	1σ	Ta	1σ	Zr	1σ	Hf	1σ
$D_{Cpx/Opx}$	4.41	7.23	6.42	18.88	2.33	2.40	4.88	3.97	5.81	6.16	4.40	2.7298
$D_{Cpx/Ol}$	1.53	0.73	3.59	3.20	26.79	10.50	–	–	329.94	388.14	167.38	–
$D_{Opx/Ol}$	0.82	0.49	1.05	0.74	10.93	5.53	0.93	0.55	61.53	64.90	17.10	–

Values in this table are averages of mineral concentration data from this study and our unpublished SWIR data, Seyler et al. (2011), Warren et al. (2009), and Le Roux et al. (2014).

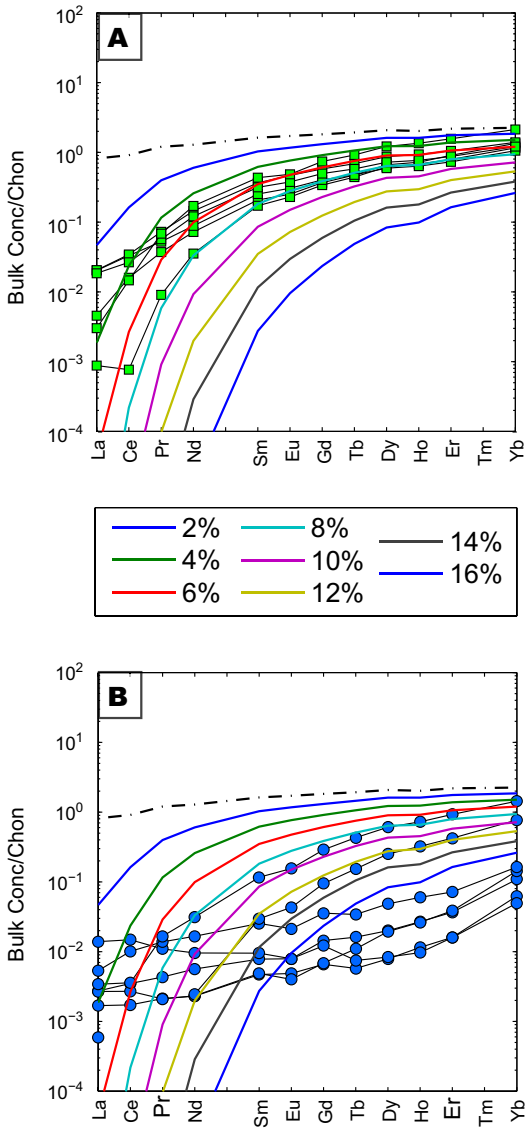

Fig. 10. Results of fractional non-modal melting model compared to calculated peridotite bulk rock compositions for (A) lherzolites and (B) harzburgites. The initial source composition, shown by the dot-dashed line, is assumed to be DMM (Workman and Hart, 2005). Partition coefficients are from Kelemen et al. (2003) and melting reaction modes are from Kinzler (1997). Gakkel bulk rock compositions were calculated from mineral modes and trace element concentrations measured in Cpx and Opx and calculated in olivine.

1 Ga, implying that large length-scale temperature variations can occur beneath mid-ocean ridges, in agreement with the recent results of Dalton et al. (2014). Hence, we conclude that implied differences in melting extents within and between dredges at the <100 km scale are not driven by thermal anomalies, as these would equilibrate in ~10–100 Ma, about the timescale of ridge processes. Instead, compositional variations at small spatial length-scales must reflect interactions with infiltrating melt, possibly overprinted on pre-existing compositional variations.

At Gakkel, the group of harzburgites with refractory compositions must be a consequence of ancient melt extrac-

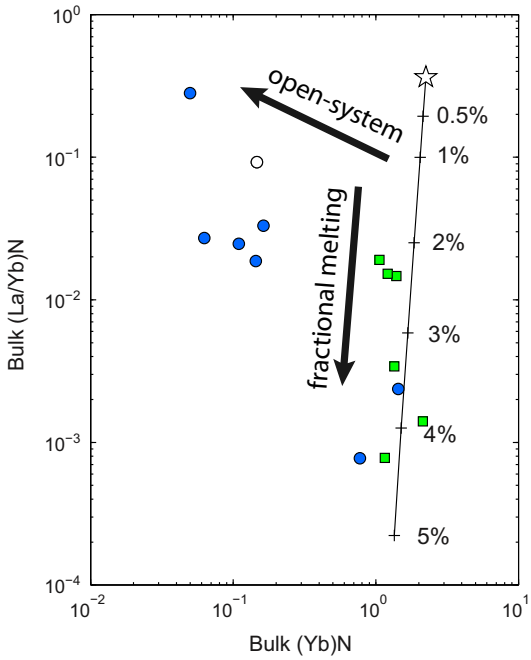

Fig. 11. Variation in Gakkel REEs expressed as $(La/Yb)_N$ vs. $(Yb)_N$. The non-modal fractional melting model from Fig. 10 is plotted as a thin black line with a starting composition represented by DMM (star). Arrow for open system melting is derived from $(La/Yb)_N$ vs. $(Yb)_N$ modeling in Brunelli et al. (2014).

tion in the mantle. However, the trace element geochemistry of Gakkel harzburgites, particularly their relatively high LREE/HREE ratios, also requires refertilization by an infiltrating melt. Next, we discuss the role of migrating melts in an open-system, which can create small length-scale geochemical variation. Refertilization of previously melted mantle has been used to explain trace element and isotopic variations observed in orogenic massifs such as Lherz (Le Roux et al., 2007), Horoman (Saal et al., 2001), Ronda (Lenoir et al., 2001) and Lanzo (Müntener et al., 2004) and in abyssal peridotites from the MAR (e.g., Brunelli et al., 2006; Godard et al., 2008) and SWIR (e.g., (Seyler et al., 2004; Warren et al., 2009; Seyler et al., 2011; Brunelli et al., 2014).

5.5. Fractional- vs. other forms of open-system melting

Fractional melting models assume that melt is instantaneously removed from the residue without interacting with the mantle. In Section 5.3, trace element variations in Gakkel lherzolites were successfully modeled by different degrees of non-modal fractional melting. In contrast, Gakkel harzburgites with the most refractory compositions (e.g. spinel Cr# = 45 – 56, Fig. 3) have LREE concentrations ($(La)_N = 0.06 – 0.18$) that are not depleted enough to be explained by fractional melting alone. In Fig. 11, the variation in $(La/Yb)_N$ as a function of Yb_N provides a representation of the significant change in slope of REE patterns among our sample set. The elevated La/Yb ratios of the harzburgites supports the theory that mantle melting is often better represented as an open-system process whereby

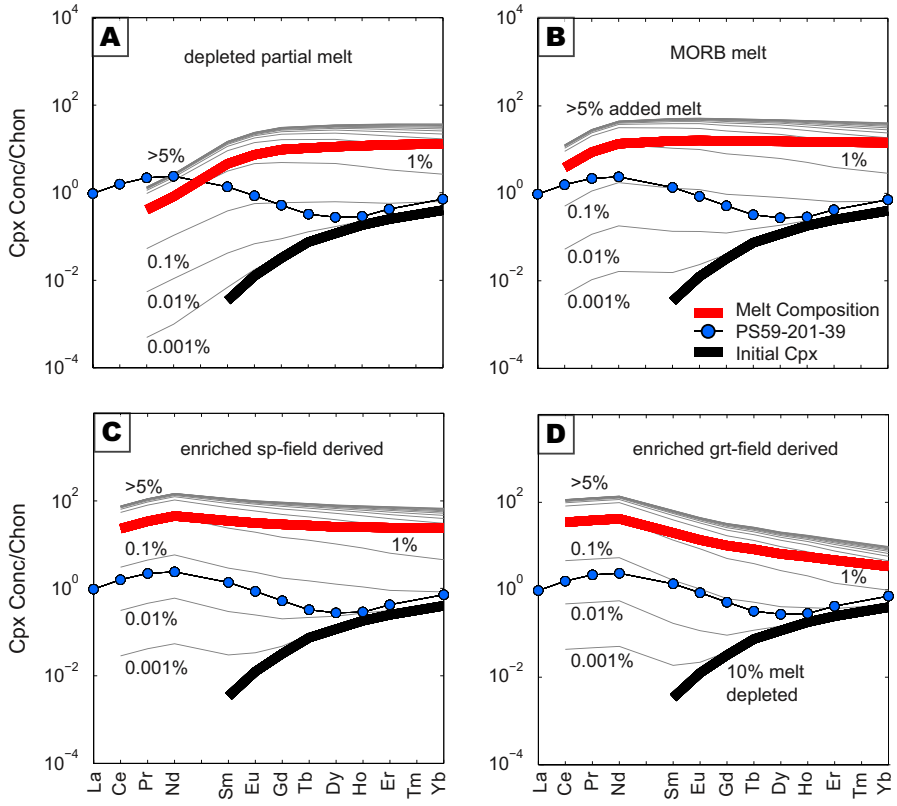

Fig. 12. Melt entrapment model showing clinopyroxene compositions normalized to chondrite (Anders and Grevesse, 1989). The model uses a depleted harzburgite starting composition with 0.1% modal Cpx (thick black line), which was calculated from 10% non-modal fractional melting in the spinel stability field of a DMM source. This initial depleted melt composition contains no initial LREE. Compositions of the trapped melt (thick red line) are from Brunelli et al. (2014) and include: (A) depleted partial melt, (B) MORB-like melt, (C) enriched melt derived from the spinel stability field and (D) enriched melt derived from the garnet stability field. In the model, the melt crystallizes as 70% Cpx and 30% olivine, which equilibrates with the pre-existing peridotite minerals (full model parameters are in Appendix C). The grey lines show the evolution of peridotite Cpx composition as the melt crystallizes, labeled with the percentage of trapped melt. At >5% trapped melt, the lines overlap and form a thick grey line. Gakkel sample PS59-201-39 Cpx is shown as blue circles. (For interpretation of the references to color in this figure legend, the reader is referred to the web version of this article.)

migrating melts chemically interact with the melting peridotite (Johnson and Dick, 1992; Ozawa and Shimizu, 1995; Godard et al., 2000; Brunelli et al., 2014).

Open-system melting involves many variables, including source composition, melt composition, melt-rock ratio, and melt addition rate (e.g., Navon and Stolper, 1987; Spiegelman, 1996; Vernières et al., 1997; Zou, 1998; Shaw, 2000; Brunelli et al., 2014). Recent modeling by Brunelli et al. (2014) reviewed the influence of these various parameters on REE concentrations. Their results show that REE patterns that cannot be generated by fractional melting alone can be reproduced by incremental open-system melting with the influx of relatively enriched melts. In this study, open-system melting provides a reasonable explanation for the LREE enrichment observed in Gakkel harzburgites (Fig. 11). Fractional partial melting fits the two least depleted harzburgites (PS59-246-01 and PS59-317-6). However, all other harzburgites form a distinct group with enrichment in LREE – shown by high $(La/Yb)_N$ – and depletion in HREE – shown by low $(Yb)_N$. This trend of increasing LREE and decreasing HREE is observed in open-system melting models (e.g., Godard et al., 2008; Brunelli et al., 2014). Hence, we propose that LREE enrichement observed in Gakkel harzburgites are a result of open-system melting and we investigate the nature of the infiltrating melts in the next section.

5.6. Nature of the interacting melt

Gakkel peridotites show other evidence for melt-rock reaction, in addition to elevated LREE concentrations among harzburgites. Petrographic evidence for refertilization and inefficiently extracted melts at shallow depths include the occurrence of spinel-orthopyroxene symplectites (HLY0102-92-36; Fig. 2E and 2F). Symplectites have been observed in ophiolites, where they have been related to melt addition to the peridotite (e.g., Rampone, 1997; Piccardo et al., 2007; Suhr et al., 2008; Marchesi et al., 2013). Symplectites have also been observed in abyssal peridotites in relation to melt-rock interaction (Morishita et al., 2007; Seyler et al., 2007), although less systematically documented. Gakkel symplectite microstructures are comparable to harzburgites from the MAR Fifteen-Twenty Fracture Zone (Seyler et al., 2007), particularly group 1

symplectites, which are suggested to have formed when melt surrounding Opx reacted to precipitate spinel and Cpx (Suhr et al., 2008). The melts that impregnated the Gakkel mantle could have failed to escape due to the thick lithospheric lid, similar to observations in abyssal peridotites at slow spreading mid-ocean ridges (e.g., Dick, 1989).

The trace element composition of harzburgite sample PS59-201-39 provides further evidence for melt refertilization of the Gakkel lithospheric mantle. Evidence for melt infiltration in this sample is indicated by the distinct Cpx REE pattern consisting of LREE>HREE, an uncommon observation in abyssal peridotites (Fig. 5). From the same dredge, a second harzburgite sample, PS59-201-40, has a REE pattern similar to all of our other harzburgites (Fig. 4). In contrast, sample PS59-201-39 shows an extreme enrichment in LREEs ($(La/Yb)_N = 1.34$). This type of REE pattern has been documented in two other Gakkel harzburgites (Fig. 5), which are also from the SMZ (D39 and D249) by Hellebrand et al. (2005). In the Indian Ocean, similar LREE enriched patterns have been observed in Cpx from a harzburgite (Hellebrand et al., 2002b) and a lherzolite (Seyler et al., 2011). In the Hellebrand et al. (2002b) study, the REE pattern was reproduced by modeling the entrapment of a small amount of refractory melt. In contrast, the lherzolite from the Seyler et al. (2011) study was modeled by open-system melting involving a highly enriched melt from a garnet-bearing source (Brunelli et al., 2014). Results of these two studies indicate the significance of the refertilizing melt composition.

To explore the nature of the infiltrating melt in our Gakkel harzburgite (PS59-201-39), we first created a harzburgitic starting composition by running the non-modal fractional melting model to 10% fractional melting. We then allowed the melt compositions of Brunelli et al. (2014; see Appendix C for the melt compositions) to crystallize in the peridotite, using the equations of Hellebrand et al. (2002b) to calculate Cpx compositions after trapping 0.001 – 15% melt (Fig. 12). Our results show that the concave-down Cpx pattern can be accounted for by entrapment of 0.1% of an enriched melt derived from either the spinel-field (Fig. 12C) or garnet-field (Fig. 12D). In addition, our modeling demonstrates that trapping a depleted partial melt (Fig. 12A) or a MORB melt (Fig. 12B) cannot explain sample PS59-201-39. We conclude that complex melt-rock interaction processes operate at short length-scales at Gakkel, creating sub-meter to kilometer scale heterogeneities in the lithospheric mantle. This implies that, despite the occurrence of refractory harzburgites in the region of dredge 201, a more fertile mantle component is also present.

Thermal models of low spreading-rate ridges predict the formation of crust-mantle mix zones when melts become trapped in the mantle (e.g., Bown and White, 1994; Sleep and Barth, 1997; Sleep and Warren, 2014). Melt freezing within the mantle produces a compositional mixture that can explain intermediate seismic velocities below the Moho (Jokat et al., 2003; Lizarralde et al., 2004; Conley and Dunn, 2011). Our observations demonstrate an enriched melt infiltrated, reacted and became trapped within residues at Gakkel Ridge in the SMZ, suggesting that the system is avolcanic, not amagmatic.

6. CONCLUSION

In this study, abyssal peridotite major and trace element compositions were measured in order to constrain mantle melting and composition beneath the Gakkel Ridge. Peridotites range from lherzolites to refractory harzburgites that are variably depleted in major and trace elements. Clinopyroxene and orthopyroxene compositions were used to calculate temperatures using the REE-in-pyroxene thermometer. Calculated temperatures >1350°C generally correspond to LREE enriched Gakkel harzburgites and are not interpreted as reflecting real temperatures. In contrast, the remainder of the Gakkel samples yield REE closure temperatures in the range of ~1100–1300°C.

Trace element modeling of the peridotites indicates varying extents of mantle melting, both within and between dredges. The high degree of partial melting modeled by peridotite geochemistry implies crustal thicknesses that are inconsistent with the thin crust observed seismically at Gakkel Ridge. In addition, geochemical variability occurs at length-scales that are too short to be thermally driven. Instead, we interpret the compositional range of Gakkel peridotites to indicate prior melting event(s) that created pre-existing compositional heterogeneity in the mantle source, along with recent melts that became trapped in the Gakkel mantle. These processes are particularly evident along the SMZ, where LREE enrichments in refractory harzburgites require both ancient melting and later melt addition. In addition, an unusual REE pattern in sample PS59-201-39 suggests crystallization of an enriched melt derived from either the spinel- or garnet-field. This demonstrates that more fertile mantle components are present and co-existing with infertile components in the Gakkel mantle. Overall, the compositional range of Gakkel samples from harzburgite to lherzolite, with geochemical variability at short length-scales, suggests that the Gakkel mantle is the consequence of inherited melt depletion and later refertilization.

ACKNOWLEDGEMENTS

At University of Montpellier, we are grateful to Benoît Ildefonse for discussions and project planning, Olivier Bruguier for technical assistance on the LA-ICPMS, and Christophe Nevado and Doriane Delmas for preparing thick sections. We thank Leslie Hayden for access to and guidance using the EMPA at the United States Geological Survey in Menlo Park. Discussion and informal reviews from Jason Harvey, Marty Grove, and Daniele Brunelli are gratefully acknowledged. Henry Dick generously provided access to the Gakkel samples and his thin sections. Eric Hellebrand is thanked for providing his melting model for use in this study and Nick Dygert for providing advance access to his manuscript. We thank Henry Dick, Eric Hellebrand and Daniele Brunelli for their thorough reviews and the editors Marc Norman and Wolfgang Bach for handling the review process. Visits between Stanford and Géosciences Montpellier were supported by funding from the France-Stanford Center for Interdisciplinary Studies. J.M.W. received support from the National Science Foundation through grant OCE-1434199.

APPENDIX A. AVERAGE MEAN RAW CPS BACKGROUND SUBSTRACTED OF REFERENCE MATERIALS USED AS EXTERNAL STANDARDS

Session date	April-2012			October-2012
Std Ref. material	NIST-SRM-612			NIST-SRM-612
Spot size	163 μm Avg. ($n = 23$)	122 μm Avg. ($n = 8$)	102 μm Avg. ($n = 32$)	122 μm Avg. ($n = 20$)
Rb	1,903,298	1,323,827	993,646	1,079,754
Sr	4,079,449	2,683,338	2,096,741	2,878,605
Y	1,559,203	990,577	775,215	1,481,264
Zr	719,267	459,319	360,682	702,327
Nb	1,487,537	992,429	778,264	1,241,293
Ba	407,123	277,888	208,847	218,733
La	1,831,744	1,236,766	956,039	1,595,115
Ce	2,058,120	1,443,761	1,077,882	1,624,845
Pr	2,664,429	1,834,286	1,406,286	1,998,231
Nd	432,366	287,385	222,026	307,913
Sm	402,048	264,044	205,331	271,676
Eu	1,387,357	937,404	729,269	853,476
Gd	436,933	280,318	227,683	247,588
Tb	2,050,164	1,357,492	1,073,245	1,555,610
Dy	477,826	310,295	244,108	347,759
Ho	1,891,619	1,236,590	979,833	1,423,181
Er	443,167	285,742	225,054	317,787
Tm	1,922,353	1,258,350	990,152	1,372,835
Yb	351,304	227,743	177,312	221,577
Lu	1,783,277	1,169,588	918,808	1,203,350
Hf	299,249	196,093	152,821	210,198
Ta	1,779,376	1,193,533	945,904	1,519,293

APPENDIX B. CALCULATED BULK ROCK COMPOSITIONS (PPM) NORMALIZED TO CHONDRITE

	La	Ce	Pr	Nd	Sm	Eu	Gd	Tb	Dy	Ho	Er	Yb
HLY0102-40-18	0.0027	0.0035	0.0043	0.0056	0.0078	0.0079	0.0144	0.0162	0.02	0.0268	0.0367	0.1091
HLY0102-40-56	0.0017	0.0017	0.0021	0.0023	0.0047	0.0049	0.0066	0.0058	0.0079	0.0115	0.016	0.0627
HLY0102-40-79	0.0027	0.0027	0.0021	0.0023	0.0049	0.004	0.0069	0.011	0.0194	0.0264	0.0386	0.1441
HLY0102-40-81	0.014	0.0148	0.011	0.0096	0.0095	0.0079	0.0122	0.0075	0.0084	0.0097	0.0159	0.0498
HLY0102-70-75	0.0046	0.016	0.0372	0.0721	0.2081	0.2515	0.3684	0.4738	0.6622	0.7221	0.9095	1.3462
HLY0102-92-36	0.0009	0.0008	0.009	0.0353	0.1716	0.2293	0.339	0.4432	0.6191	0.6783	0.7947	1.1566
PS59-201-39	0.0135	0.0221	0.0341	0.0407	0.0287	0.0202	0.0171	0.0128	0.0143	0.0211	0.0393	0.1466
PS59-201-40	0.0054	0.0101	0.0138	0.0167	0.0255	0.0212	0.0356	0.0342	0.0484	0.0601	0.0719	0.1633
PS59-235-01	0.0202	0.0332	0.0524	0.0884	0.2536	0.3051	0.4034	0.4751	0.5934	0.634	0.7303	1.0592
PS59-235-17	0.0205	0.0343	0.0728	0.1449	0.366	0.4664	0.5801	0.6871	0.8665	0.9334	1.0529	1.3956
PS59-235-18	0.0184	0.0266	0.0568	0.1209	0.3155	0.3761	0.497	0.5796	0.7241	0.7668	0.8743	1.2088
PS59-238-75	0.003	0.0146	0.0682	0.1711	0.4335	0.4857	0.7426	0.9208	1.2179	1.3524	1.5673	2.1356
PS59-246-01	0.0034	0.0036	0.0166	0.0313	0.1163	0.156	0.2893	0.4309	0.6086	0.7253	0.9265	1.4377
PS59-317-6	0.0006	b.d.	b.d.	0.0025	0.0297	0.0432	0.0948	0.154	0.2509	0.3238	0.4243	0.7747

b.d. = analysis was below detection limit.

APPENDIX C. INPUT PARAMETERS FOR MELT ENTRAPMENT MODEL

	Intial Cpx	Melt composition						
		Enriched grt-derived (1% melt of DMM Grt lherz Brunelli et al. (2014))	Midly enriched sp-derived (1% melt of DMM in spinel-field Brunelli et al. (2014))	Depleted (1% melt after 4% grt +10% sp Brunelli et al. (2014)	Aggregated MORB-like (4% grt + 10% sp) Brunelli et al. (2014)	Depleted melt Hellebrand et al. (2002b)		Initial modes
La	0.000					0.000	Ol	0.850
Ce	0.000	21.123	13.990	0.000	2.347	0.110	Opx	0.139
Pr	0.000						Cpx	0.001
Nd	0.000	19.001	20.358	0.371	6.153	0.770	Sp	0.010
Sm	0.001	2.942	5.149	0.677	2.324	0.630		
Eu	0.001	0.773	1.736	0.414	0.904	0.330		
Gd	0.006	2.005	5.701	1.897	3.106			
Tb	0.003							
Dy	0.029	1.602	6.189	2.745	3.725	1.770		
Ho	0.008							
Er	0.039	0.755	3.895	1.970	2.352	1.190		
Yb	0.065	0.553	3.864	2.126	2.337	1.220		

Initial residual Cpx composition was calculated from 10% non-modal fractional melting from model in Fig. 8.
Initial modes of depleted mantle composition from Hellebrand et al. (2002b).
Melt compositions are from Brunelli et al. (2014) in Table 1.

REFERENCES

Anders E. and Grevesse N. (1989) Abundances of the elements: meteoritic and solar. *Geochim. Cosmochim. Acta* **53**, 197–214.

Bown J. W. and White R. S. (1994) Variation with spreading rate of oceanic crustal thickness and geochemistry. *Earth Planet. Sci. Lett.* **121**, 435–449.

Brey G. and Köhler T. (1990) Geothermobarometry in four-phase lherzolites II. New thermobarometers, and practical assessment of existing thermobarometers. *J. Petrol.* **31**, 1353–1378.

Brunelli D., Paganelli E. and Seyler M. (2014) Percolation of enriched melts during incremental open-system melting in the spinel field: a REE approach to abyssal peridotites from the Southwest Indian Ridge. *Geochim. Cosmochim. Acta* **127**, 190–203.

Brunelli D., Seyler M., Cipriani A., Ottolini L. and Bonatti E. (2006) Discontinuous melt extraction and weak refertilization of mantle peridotites at the vema lithospheric section (Mid-Atlantic Ridge). *J. Petrol.* **47**, 745–771.

Byerly B. L. and Lassiter J. C. (2014) Isotopically ultradepleted domains in the convecting upper mantle: implications for MORB petrogenesis. *Geology*.

Cannat, M. (1996) How thick is the magmatic crust at slow spreading oceanic ridges? Melt Migration in the Axial Lithosphere of Slow Spreading Ridges: Constraints from Ultramafic and Gabbroic Samples. **101**, 2847–2857.

Chen Y. (1992) Oceanic crustal thickness versus spreading rate. *Geophys. Res. Lett.*, 753–756.

Coakley B. and Cochran J. (1998) Gravity evidence of very thin crust at the Gakkel Ridge (Arctic Ocean). *Earth Planet. Sci. Lett.* **162**, 81–95.

Cochran J. R., Kurras G. J., Edwards M. H. and Coakley B. J. (2003) The Gakkel Ridge: bathymetry, gravity anomalies, and crustal accretion at extremely slow spreading rates. *J. Geophys. Res.* **108**, 2116.

Conley M. M. and Dunn R. a. (2011) Seismic shear wave structure of the uppermost mantle beneath the Mohns Ridge. *Geochem. Geophys. Geosyst.* **12**, 1–15.

Craddock P. R., Warren J. M. and Dauphas N. (2013) Abyssal peridotites reveal the near-chondritic Fe isotopic composition of the Earth. *Earth Planet. Sci. Lett.* **365**, 63–76.

Dalton C. a., Langmuir C. H. and Gale A. (2014) Geophysical and geochemical evidence for deep temperature variations beneath mid-ocean ridges. *Science* **344**, 80–83.

Dick H. J. B. (1989) Abyssal peridotites, very slow spreading ridges and ocean ridge magmatism. *Geol. Soc. Lond.* **42**, 71–105 (Spec. Publ.).

Dick H. J. B., Lin J. and Schouten H. (2003) An ultraslow-spreading class of ocean ridge. *Nature* **426**, 405–412.

Dick H. J. B., Snow J. E., Michael P. J., Hellebrand E., Shimizu N. and Hofmann A. W. (2004) Gakkel Ridge: mantle and melting at ultraslow spreading rates. *Geochim. Cosmochim. Acta* **68** (Supplement), 691.

Dygert N. and Liang Y. (2015) Temperatures and cooling rates recorded in REE in coexisting pyroxenes in ophiolitic and abyssal peridotites. *Earth Planet. Sci. Lett.* **420**, 151–161.

Elkins L. J., Sims K. W. W., Prytulak J., Blichert-Toft J., Elliott T., Blusztajn J., Fretzdorff S., Reagan M., Haase K., Humphris S. and Schilling J.-G. (2013) Melt generation beneath Arctic Ridges: implications from U decay series disequilibria in the Mohns, Knipovich, and Gakkel Ridges. *Geochim. Cosmochim. Acta*.

Forsyth D. W. (1993) Crustal thickness and the average depth and degree of melting in fractional melting models of passive flow beneath mid-ocean ridges. *J. Geophys. Res. Solid Earth* **98**.

Gale A., Dalton C. A., Langmuir C. H., Su Y. and Schilling J.-G. (2013) The mean composition of ocean ridge basalts. *Geochem. Geophys. Geosyst.* **14**, 489–518.

Gibert B. (2003) Thermal diffusivity of upper mantle rocks: influence of temperature, pressure, and the deformation fabric. *J. Geophys. Res.* **108**, 2359.

Godard M., Jousselin D. and Bodinier J.-L. (2000) Relationships between geochemistry and structure beneath a palaeo-spreading centre: a study of the mantle section in the Oman ophiolite. *Earth Planet. Sci. Lett.* **180**, 133–148.

Godard M., Lagabrielle Y., Alard O. and Harvey J. (2008) Geochemistry of the highly depleted peridotites drilled at ODP Sites 1272 and 1274 (Fifteen-Twenty Fracture Zone, Mid-Atlantic Ridge): implications for mantle dynamics beneath a slow spreading ridge. *Earth Planet. Sci. Lett.* **267**, 410–425.

Goldstein S. L., Soffer G., Langmuir C. H., Lehnert K., Graham D. W. and Michael P. J. (2008) Origin of a "Southern Hemisphere" geochemical signature in the Arctic upper mantle. *Nature* **453**, 89–93.

Günther D. and Heinrich C. (1999) Enhanced sensitivity in laser ablation-ICP mass spectrometry using helium–argon mixtures as aerosol carrier. *J. Anal. At. Spectrom.* **14**, 1363–1368.

Hart S. R. and Dunn T. (1993) Experimental Cpx/melt partitioning of 24 trace elements. *Contrib. Mineral. Petrol.* **113**, 1–8.

Harvey J., Gannoun A., Burton K. W., Rogers N. W., Alard O. and Parkinson I. J. (2006) Ancient melt extraction from the oceanic upper mantle revealed by Re–Os isotopes in abyssal peridotites from the Mid-Atlantic ridge. *Earth Planet. Sci. Lett.* **244**, 606–621.

Hellebrand E., Snow J. E. and Mühe R. (2002a) Mantle melting beneath Gakkel Ridge (Arctic Ocean): abyssal peridotite spinel compositions. *Chem. Geol.* **182**, 227–235.

Hellebrand E., Snow J. E., Hoppe P. and Hofmann A. W. (2002b) Garnet-field melting and late-stage refertilization in "residual" abyssal peridotites from the Central Indian Ridge. *J. Petrol.* **43**, 2305–2338.

Hellebrand E., Snow J. E., Mostefaoui S. and Hoppe P. (2005) Trace element distribution between orthopyroxene and clinopyroxene in peridotites from the Gakkel Ridge: a SIMS and NanoSIMS study. *Contrib. Mineral. Petrol.* **150**, 486–504.

Horai K. and Susaki J. (1989) The effect of pressure on the thermal conductivity of silicate rocks up to 12 kbar. *Phys. Earth Planet. Inter.* **55**, 292–305.

Jackson H. R., Reid I. and Falconer R. K. H. (1982) Crustal structure near the Arctic mid-ocean ridge. *J. Geophys. Res.* **87**, 1773–1783.

Jochum K. P., Stoll B., Herwig K., Amini M., Abouchami W. and Hofmann a. W. (2005) Lead isotope ratio measurements in geological glasses by laser ablation-sector field-ICP mass spectrometry (LA-SF-ICPMS). *Int. J. Mass Spectrom.* **242**, 281–289.

Johnson K. and Dick H. J. B. (1992) Open system melting and temporal and spatial variation of peridotite and basalt at the Atlantis II Fracture Zone. *J. Geophys. Res.* **97**, 9219.

Johnson K., Dick H. J. B. and Shimizu N. (1990) Melting in the oceanic upper mantle: an ion microprobe study of diopsides in abyssal peridotites. *J. Geophys. Res.* **95**, 2661–2678.

Jokat W., Ritzmann O., Schmidt-Aursch M. C., Drachev S., Gauger S. and Snow J. (2003) Geophysical evidence for reduced melt production on the Arctic ultraslow Gakkel mid-ocean ridge. *Nature* **423**, 962–965.

Jokat W. and Schmidt-Aursch M. C. (2007) Geophysical characteristics of the ultraslow spreading Gakkel Ridge, Arctic Ocean. *Geophys. J. Int.* **168**, 983–998.

Kelemen P., Shimizu N. and Dunn T. (1993) Relative depletion of niobium in some arc magmas and the continental crust: partitioning of K, Nb, La and during melt/rock reaction in the upper mantle. *Earth Planet. Sci. Lett.* **120**, 111–134.

Kelemen P., Yogodzinski G. and Scholl D. (2003) Along-strike variation in the Aleutian island Arc genesis of high Mg# andesite and implications for continental crust. *Geophys. Monogr. Ser.*

Kinzler R. J. (1997) Melting of mantle peridotite at pressures approaching the spinel to garnet transition: application to mid-ocean ridge basalt petrogenesis. *J. Geophys. Res.* **102**, 853.

Klein E. M. and Langmuir C. H. (1987) Global correlations of ocean ridge basalt chemistry with axial depth and crustal thickness. *J. Geophys. Res.* **92**, 8089–8115.

Lenoir X., Garrido C., Bodinier J., Dautria J. M. and Gervilla F. (2001) The recrystallization front of the Ronda peridotite: evidence for melting and thermal erosion of subcontinental lithospheric mantle beneath the Alboran Basin. *J. Petrol.* **42**, 141–158.

Le Roux V., Bodinier J. L., Tommasi A., Alard O., Dautria J.-M., Vauchez A. and Riches A. J. V. (2007) The Lherz spinel lherzolite: refertilized rather than pristine mantle. *Earth Planet. Sci. Lett.* **259**, 599–612.

Le Roux V., Dick H. J. B. and Shimizu N. (2014) Tracking flux melting and melt percolation in supra-subduction peridotites (Josephine ophiolite, USA). *Contrib. Mineral. Petrol.* **168**.

Liang Y., Sun C. and Yao L. (2013) A REE-in-two-pyroxene thermometer for mafic and ultramafic rocks. *Geochim. Cosmochim. Acta* **102**, 246–260.

Liu C. Z., Snow J. E., Hellebrand E., Brügmann G., von der Handt A., Büchl A. and Hofmann A. W. (2008a) Ancient, highly heterogeneous mantle beneath Gakkel Ridge, Arctic Ocean. *Nature* **452**, 311–316.

Liu Y., Hu Z., Gao S., Gunther D., Xu J., Gao C. and Chen H. (2008b) In situ analysis of major and trace elements of anhydrous minerals by LA-ICP-MS without applying an internal standard. *Chem. Geol.* **257**, 34–43.

Lizarralde D., Gaherty J., Collins J., Hirth G. and Kim S. (2004) Spreading-rate dependence of melt extraction at mid-ocean ridges from mantle seismic refraction data. *Nature* **432**, 7–10.

MacGregor I. D. I. D. (2015) Empirical geothermometers and geothermobarometers for spinel peridotite phase assemblages. *Int. Geol. Rev.*, 1–35.

Malaviarachchi S. P. K., Makishima A., Tanimoto M., Kuritani T. and Nakamura E. (2008) Highly unradiogenic lead isotope ratios from the Horoman peridotite in Japan. *Nat. Geosci.* **1**, 859–863.

Michael P. J., Langmuir C. H., Dick H. J. B. and Snow J. E. (2003) Magmatic and amagmatic seafloor generation at the ultraslow-spreading Gakkel ridge, Arctic Ocean. *Nature* **423**, 956–961.

Michael P. J., Langmuir C. H., Goldstein S. L., Soffer G., Dick H. J. B., Snow J. E. and Graham D. W. (2004) Geochemistry of Gakkel Ridge. *Geochim. Cosmochim. Acta* **68**(Supplement), 692.

Montési L. G. J. and Behn M. D. (2007) Mantle flow and melting underneath oblique and ultraslow mid-ocean ridges. *Geophys. Res. Lett.* **34**, L24307.

Morishita T., Maeda J., Miyashita S., Kumagai H., Matsumoto T. and Dick H. J. B. (2007) Petrology of local concentration of chromian spinel in dunite from the slow-spreading Southwest Indian Ridge. *Eur. J. Mineral.* **19**, 871–882.

Mühe R., Devey C. W. and Bohrmann H. (1993) Isotope and trace element geochemistry of MORB from the Nansen-Gakkel ridge at 86° north. *Earth Planet. Sci. Lett.* **120**, 103–109.

Mühe R. K., Bohrmann H., Hörmann P. K., Thiede J. and Stoffers P. (1991) Spinifex basalts with komatiite-tholeiite trend from the Nansen-Gakkel Ridge (Arctic Ocean). *Tectonophysics* **190**, 95–108.

Mühe R., Peucker-Ehrenbrink B., Devey C. W. and Garbe-Schönberg D. (1997) On the redistribution of Pb in the oceanic crust during hydrothermal alteration. *Chem. Geol.* **137**, 67–77.

Müntener O., Pettke T., Desmurs L., Meier M. and Schaltegger U. (2004) Refertilization of mantle peridotite in embryonic ocean basins: trace element and Nd isotopic evidence and implications for crust–mantle relationships. *Earth Planet. Sci. Lett.* **221**, 293–308.

Navon O. and Stolper E. (1987) Geochemical consequences of melt percolation: the upper mantle as a chromatographic column. *J. Geol.* **95**.

Ozawa K. and Shimizu N. (1995) Open-system melting in the upper mantle: constraints from the Hayachine–Miyamori ophiolite, Northeastern Japan. *J. Geophys. Res. Solid Earth* **100**, 22315–22335.

Pearce N. J. G., Perkins W. T., Westgate J. a., Gorton M. P., Jackson S. E., Neal C. R. and Chenery S. P. (1997) A compilation of new and published major and trace element data for NIST SRM 610 and NIST SRM 612 glass reference materials. *Geostand. Geoanal. Res.* **21**, 115–144.

Piccardo G. B., Zanetti a. and Müntener O. (2007) Melt/peridotite interaction in the Southern Lanzo peridotite: field, textural and geochemical evidence. *Lithos* **94**, 181–209.

Rampone E. (1997) Chemistry and origin of trapped melts in ophiolitic peridotites. *Geochim. Cosmochim. Acta* **61**, 4557–4569.

Reid I. and Jackson H. R. (1981) Oceanic spreading and crustal thickness. *Mar. Geophys. Res.* **5**, 165–172.

Ryan W. B. F., Carbotte S. M., Coplan J. O., O'Hara S., Melkonian A., Arko R., Weissel R. A., Ferrini V., Goodwillie A., Nitsche F., Bonczkowski J. and Zemsky R. (2009) Global multi-resolution topography synthesis. *Geochem. Geophys. Geosyst.* **10**, 1–9.

Saal A., Takazawa E. and Frey F. (2001) Re–Os isotopes in the Horoman peridotite: evidence for refertilization? *J. Petrol.* **42**, 25–37.

Salters V. J. M., Sach-Kocher A. and Dick H. J. B. (2012) Ultra depleted mantle at the Gakkel Ridge. *Mineral. Mag.* **76**, 2317.

Seyler M., Brunelli D., Toplis M. J. and Mével C. (2011) Multiscale chemical heterogeneities beneath the eastern Southwest Indian Ridge (52°E–68°E): trace element compositions of along-axis dredged peridotites. *Geochem. Geophys. Geosyst.* **12**, Q0AC15.

Seyler M., Lorand J. P., Dick H. J. B. and Drouin M. (2007) Pervasive melt percolation reactions in ultra-depleted refractory harzburgites at the Mid-Atlantic Ridge, 15° 20′N: ODP Hole 1274A. *Contrib. Mineral. Petrol.* **153**, 303–319.

Seyler M., Lorand J. P., Toplis M. J. and Godard G. (2004) Asthenospheric metasomatism beneath the mid-ocean ridge: evidence from depleted abyssal peridotites. *Geology* **32**, 301–304.

Shaw D. M. (2000) Continuous (dynamic) melting theory revisited. *Can. Mineral.* **38**, 1041–1063.

Shaw D. M. (1970) Trace element fractionation during anatexis. *Geochim. Cosmochim. Acta* **34**, 237–243.

Shen Y. and Forsyth D. W. (1995) Geochemical constraints on initial and final depths of melting beneath mid-ocean ridges. *J. Geophys. Res.* **100**, 2211–2237.

Sleep N. H. and Barth G. a. (1997) The nature of oceanic lower crust and shallow mantle emplaced at low spreading rates. *Tectonophysics* **279**, 181–191.

Sleep N. and Warren J. (2014) Effect of latent heat of freezing on crustal generation at low spreading rates. *Geochem. Geophys.*, 3161–3174.

Snow J. E., Dick H. J. B., Hellebrand E., Buchl A., von der Handt A. and Langmuir C. H. (2002) Geochemistry of abyssal peridotites from Gakkel Ridge, Arctic Ocean. *Geochim. Cosmochim. Acta* **66**, 722.

Soffer G., Goldstein S. L., Graham D. W., Langmuir C. H. and Michael P. J. (2004) An arctic mantle domain boundary: evidence from the Gakkel Ridge. *Geochim. Cosmochim. Acta* **68** (Supplement), 692.

Spiegelman M. (1996) Geochemical consequences of melt transport in 2-D: sensitivity of trace elements to mantle dynamics. *Earth Planet. Sci. Lett.*, 1–18.

Stracke A., Snow J. E., Hellebrand E., von der Handt A., Bourdon B., Birbaum K. and Günther D. (2011) Abyssal peridotite Hf isotopes identify extreme mantle depletion. *Earth Planet. Sci. Lett.* **308**, 359–368.

Suhr G., Kelemen P. and Paulick H. (2008) Microstructures in Hole 1274A peridotites, ODP Leg 209, Mid-Atlantic Ridge: Tracking the fate of melts percolating in peridotite as the lithosphere is intercepted. *Geochem. Geophys. Geosyst.* **9**, 1–23.

Sun S.-s. and McDonough W. F. (1989) Chemical and isotopic systematics of oceanic basalts: implications for mantle composition and processes. *Geol. Soc. Lond.* **42**, 313–345 (Spec. Publ.).

Taylor W. R. (1998) An experimental test of some geothermometer and geobaromater formulations for upper mantle peridotites with application to the thermobarometry of fertile lherzolite and garnet websterite. *Neues Jahrb. Mineral. Abh.* **172**, 381–408.

Van Achterberg E., Ryan C. G., Jackson S. E. and Griffin W. (2001) Data reduction software for LA-ICP-MS. In *Laser Ablation ICP-MS in the Earth Science*, 40 (ed. P. Sylvester), pp. 239–243.

Vernières J., Godard M. and Bodinier J. L. (1997) A plate model for the simulation of trace element fractionation during partial melting and magma transport in the Earth's upper mantle. *J. Geophys. Res.* **102**, 24771–24784.

von der Handt A., Snow J. E., Hellebrand E., Dick H. J. B. and Michael P. J. (2003) Shallow mantle melt stagnation under Gakkel Ridge. *Geophys. Res. Abstr.* **5**, 11703.

von der Handt A. (2008) *Deciphering Petrological Signatures of Reactive Melt Stagnation and Cooling in the Oceanic Mantle Underneath Ultraslow-Spreading Ridges*. Ph.D. Dissertation, Johannes-Gutenberg Universität, Mainz.

Vogt P. R., Taylor P. T., Kovacs L. C. and Johnson G. L. (1979) Detailed aeromagnetic investigation of the Arctic Basin. II. *J. Geophys. Res.* **84**, 1071–1089.

Warren J. M., Shimizu N., Sakaguchi C., Dick H. J. B. and Nakamura E. (2009) An assessment of upper mantle heterogeneity based on abyssal peridotite isotopic compositions. *J. Geophys. Res.* **114**, 1–36.

Warren J. M. and Shirey S. B. (2012) Lead and osmium isotopic constraints on the oceanic mantle from single abyssal peridotite sulfides. *Earth Planet. Sci. Lett.* **359–360**, 279–293.

Weigelt E. and Jokat W. (2001) Peculiarities of roughness and thickness of oceanic crust in the Eurasian Basin, Arctic Ocean. *Geophys. J. Int.* **145**, 505–516.

Wells P. R. A. (1977) Pyroxene thermometry in simple and complex systems. *Contrib. Mineral. Petrol.* **62**, 129–139.

White R. S., McKenzie D. and O'Nions K. (1992) Oceanic crustal thickness from seismic measurements and rare earth element inversions. *J. Geophys. Res.* **97**.

White R. S., Minshull T. A., Bickle M. J. and Robinson C. J. (2001) Melt generation at very slow-spreading oceanic ridges: constraints from geochemical and geophysical data. *J. Petrol.* **42**, 1171–1196.

Witt-Eickschen G. and Seck H. (1991) Solubility of Ca and Al in orthopyroxene from spinel peridotite: an improved version of an empirical geothermometer. *Contrib. Mineral. Petrol.*, 431–439.

Workman R. K. and Hart S. R. (2005) Major and trace element composition of the depleted MORB mantle (DMM). *Earth Planet. Sci. Lett.* **231**, 53–72.

Zou H. (1998) Trace element fractionation during modal and nonmodal dynamic melting and open-system melting: a mathematical treatment. *Geochim. Cosmochim. Acta* **62**, 1937–1945.

Associate editor: Wolfgang Bach